journal of the international meteor organization

WGN

46:2
april 2018

Fundamentals of infrasound observations of bright meteors
Simultaneous radiometric and video observations of fireballs
Raspberry Pi based meteor camera system results
Discovery of the Alpha Aquariids
Estimating directions of meteors from static images
Outburst of the February Hydrids

ISSN 1016-3115

WGN Vol. 46, No. 2, April 2018, pp. 51 – 86

Administrative

Meteor Science

Short communication

Front cover photo

Lyrid fireball captured on 2015 April 21 at $01^{\mathrm{h}}14^{\mathrm{m}}$ UT from Ližnjan, Croatia. Canon 6D was used with Samyang 24 mm lens at $f/2.0$, and 13 s exposure at ISO 3200. Photo courtesy: Marko Korošec.

Writing for WGN

This Journal welcomes papers submitted for publication. All papers are reviewed for scientific content, and edited for English and style. Instructions for authors can be found in WGN **45:1**, 1–5, and at `http://www.imo.net/docs/writingforwgn.pdf` .

Legal address

International Meteor Organization, Jozef Mattheessensstraat 60, 2540 Hove, Belgium.

News from the IMO Council

Cis Verbeeck[1]

After the 2017 IMO Council elections, the IMO Council appointed the new IMO Board members. Bob Lunsford and Marc Gyssens were re-elected as Secretary-General and Treasurer, respectively. Jürgen Rendtel had indicated that he would like to hand over the function of Vice President. The IMO Council is glad to announce that Juraj Tóth is our new Vice President.

On behalf of the IMO Council, I would like to thank Jürgen for his excellent contributions as Vice President, in a time which was not always easy and when sometimes bold decisions had to be taken. Of course, Jürgen will continue to contribute to IMO as Council member and through the various tasks that he performs for IMO.

Again on behalf of the IMO Council, I would like to wish our new Vice President Juraj Tóth a lot of success in the years ahead! I am convinced that Juraj will do a great job, enriching the IMO Board with new ideas and vantage points.

IMO bibcode WGN-462-verbeeck-news NASA-ADS bibcode 2018JIMO...46...51V

Erratum: The Efficiency of Cameras for Video Meteor Observation – A theoretical contribution and a practical comparison between the Watec 120N+ and the Sony α7S

The WGN Editorial Team

In the 46:1 issue of WGN, Journal of the International Meteor Organization, an article was published comparing efficiencies of Watec 120N+ and Sony α7S cameras (Slansky, 2018). On page 25, below formula (2), the correct value of c_{ISO} (ISO calibration factor) is 285 lux s, not 228 lux s as given in the article. Both values (and also others, such as 250 lux s) had been in use in the past, but all calculations in the article are based on $c_{\mathrm{ISO}} = 285$ lux s, which is the one used mostly.

We sincerely apologize to our readers.

References

Slansky P. C. (2018). "The Efficiency of Cameras for Video Meteor Observation – A theoretical contribution and a practical comparison between the Watec 120N+ and the Sony α7S". *WGN, Journal of the IMO*, **46:1**, 24–29.

IMO bibcode WGN-462-erratum NASA-ADS bibcode 2018JIMO...46...51W

[1] Bogaertsheide 5, 2560 Kessel, Belgium.
Email: cis.verbeeck@scarlet.be

Meteor Science

Infrasound observations of bright meteors: the fundamentals

Elizabeth A. Silber [1]

Meteors are produced by extraterrestrial solid particles as they enter the Earth's atmosphere at high velocities. These particles, ranging from sub-millimeter to centimeter-sized objects—and very rarely also objects up to tens of meters—can produce a range of phenomena, from intense light to destructive shock waves that could inflict significant damage on the ground. Meteor-generated shock waves decay into very low-frequency acoustic (infrasonic) waves at long distances from the source, and can propagate over many kilometers (hundreds to thousands) and may eventually be detected on the ground by sensitive microphones. Infrasound has gained considerable interest in recent decades in the civilian domain as a valuable tool in the detection of meteor-generated shock waves. While meteor phenomena cannot be completely replicated or produced in a controlled environment, installations of dedicated infrasound stations combined with all-sky networks can provide valuable information about meteoroids.

Received 2018 March 6

1 Introduction

On a daily basis, the Earth is bombarded with extraterrestrial material, collectively called meteoroids, ranging in size from micrometers to several decimeters (Brownlee, 1985). Larger objects, meters to tens of meters in size, impact less frequently, and are capable of causing damage and even casualties on the ground. Meteoroids with sufficient sizes and velocities that survive the ablative mass loss in the upper atmosphere and end up reaching the Earth's surface (at that stage referred to as meteorites) can provide us with valuable information about their parent bodies, the origins of our Solar System and possible delivery mechanisms of organic molecules to the early Earth.

Meteoroids enter the Earth's atmosphere at hypersonic velocities (v_∞) of 11–72 km/s (Ceplecha et al., 1998), which translate to Mach numbers (defined as the ratio of the meteoroid velocity to the local speed of sound) M_∞ of 35–270. During the meteoroid's passage through the Earth's atmosphere, the collisions with atmospheric particles lead to frictional heating, sputtering, evaporation, ablation, and even fragmentation. The resulting luminous phenomenon is a meteor. Very bright meteors, typically brighter than Venus (magnitude -4) are referred to as fireballs or bolides. Extremely bright events, exceeding magnitude -17, are called superbolides (Ceplecha et al., 1998). Meteors can also produce audible phenomena, which can take place almost instantaneously (electrophonic sound, e.g., Wylie, 1932; Keay, 1980; Spalding et al., 2017; and references therein) or after some delay. The latter is associated with the shock wave, similar to that produced by an aircraft when it breaks the sound barrier ("sonic boom"), and can be detected at the ground at large distances from the source in the form of low frequency sound, also called infrasound (Ceplecha et al., 1998).

[1]Department of Earth, Environmental and Planetary Sciences, Brown University, Providence, RI 02912, USA
Email: esilber@uwo.ca, elizabeth_silber@brown.edu

IMO bibcode WGN-462-silber-infrasound
NASA-ADS bibcode 2018JIMO...46...52S

The most commonly used method to study meteors are optical and radar observations. For example, multi-station all-sky camera systems can provide a range of useful information, such as meteoroid entry velocity, trajectory, orbital information, and light emission (e.g., Ceplecha et al., 1998; Weryk et al., 2007). With more attention being given to meteor events in recent decades, a number of all-sky camera networks have been set up around the globe, both in the academic and amateur domains. However, such installations have intrinsic limitations, including limitations on geographical placement and dependency on weather conditions, and are only effective during night-time observations. Another, less frequently used method to detect meteors, is via low-frequency acoustic wave emissions (infrasound) produced during the meteoroid's passage through the atmosphere. An all-sky camera network, complemented by an infrasound array installation, can provide a broader and more comprehensive picture about meteors, including the energy they produce (Edwards et al., 2008; Silber and Brown, 2014). Additionally, an infrasound array inherently has the capability to detect very distant and energetic bolides, as well as other anthropogenic and natural impulsive sources in the atmosphere (e.g., shuttle launches, mining activity, storms).

This paper aims to present a brief overview of infrasound and its applications to detections of meteor events. Very energetic events generating infrasound on a global scale are rare. Due to their unique nature, such events are well documented and presented in literature (e.g., Brown et al., 2013). Consequently, this paper discusses applications of infrasound to small (and more frequent) events that could be recorded on a regional scale on a day-to-day basis (e.g., Edwards et al., 2008; Silber and Brown, 2014).

The content of the paper is organized as follows: an overview of meteor physics is provided in Section 2, meteor-generated shock waves, infrasound, and infrasound arrays are described in Section 3, and infrasound detection of meteors is presented in Section 4. The paper concludes with Section 5, which gives an outline of future work.

2 A brief overview of meteor physics

2.1 Flow regimes and shock waves

As a meteoroid enters the upper atmosphere (approximately 150 km), it starts to heat up as a result of collisions with the rarified atmosphere and subsequently sputters. Further down, in the denser atmosphere below about 100 km, the meteoroid undergoes intense ablation. This process is also dependent on the meteoroid's size and velocity. For example, particles associated with the high-speed Leonid meteor shower ($v_\infty \approx 72$ km/s) have been known to produce luminous phenomena at altitudes above 150 km (Popova et al., 2001). There are three main flow regimes, defined by the ratio of the molecular mean free path to the meteoroid diameter (d_m), also called the Knudsen number (Kn). These flow regimes are (1) the free molecular flow (Kn > 10); (2) the transitional flow ($0.01 \leq$ Kn ≤ 10); and (3) the continuum flow (Kn < 0.01) (Ceplecha et al., 1998; Popova et al., 2001; Campbell-Brown and Koschny, 2004). In order for the shock wave to form, the meteoroid has to be sufficiently large and fast, and penetrate deep enough into the dense atmosphere while strongly ablating to reach the locally defined continuum regime within the meteor flow field (Silber et al., 2017). Typically, for bright meteors, this occurs at altitudes below about 90 km (Popova, 2005), although there are exceptions (Silber and Brown, 2014).

As a meteoroid travels at speeds much greater than the local speed of sound, it deposits a significant fraction of its energy in the form of a hypersonic shock wave. Meteors are treated as explosive line sources because of the high rate of energy deposition per unit length. In simple terms, as an object moves through the air, it creates a series of pressure waves in front of it and behind it. These waves travel at the speed of sound; however, since the speed of the meteoroid is much higher than the local speed of sound, the waves are compressed, eventually merging into a single, nearly cylindrical shock wave with a narrow Mach cone. The Mach cone angle (η) is defined by $\sin\eta = 1/\mathrm{M}_\infty$, and, in the case of meteors, it is very small ($\eta < 1\overset{\circ}{.}7$). Consequently, this is the reason that the shock wave can be quite reasonably approximated as a cylinder (Figure 1). If the meteoroid fragments, then it will generate a shock wave that can be approximated as a point-like explosion (Figure 1) (e.g., ReVelle, 1976; Ceplecha et al., 1998). The highly non-linear shock created during a meteoroid's passage through the atmosphere can be remotely sensed at the surface as a long-distance weak shock (or linear acoustic wave) (ReVelle, 1974). The original fundamental frequency, acoustic wave amplitude, and acoustic energy deposition are closely related to the shock production mechanism (ReVelle, 1976). Only a small portion of the total energy of the meteoroid will go into light emission.

2.2 Entry dynamics

In this section, only single-body ablation is considered in the context of the entry dynamics. While fragmentation is also an important phenomena during the meteoroid mass loss process (e.g., Ceplecha et al., 1998),

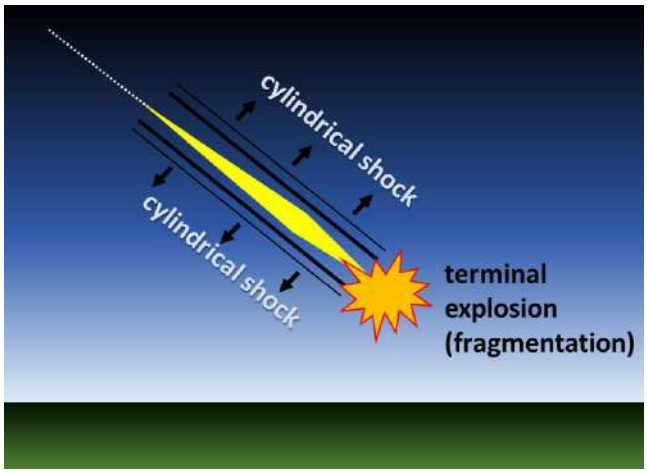

Figure 1 – Diagram showing the cylindrical line source and a fragmentation event.

it is beyond the scope of this paper. Let us consider a spherical meteoroid with the following attributes: mass (m), radius (r), density (ρ), velocity (v), cross-sectional surface area (S), drag coefficient (Γ), shape factor (A_s). The shape factor varies according to the object shape. For example, $A_\mathrm{s} = 1.209$ for a sphere; $A_\mathrm{s} = 1.0$ for a cube moving face on; and $A_\mathrm{s} = 1.92$ for a hemisphere (McKinley, 1961; Bronshten, 1983). A rotating body with an irregular shape can be approximated as a sphere. Other parameters relevant for the discussion are air mass (m_a), air density (ρ_a), the heat of ablation of the meteoroid material (energy required to ablate a unit mass of the meteoroid, ξ), and the heat transfer coefficient (a measure of efficiency of the collision process in converting kinetic energy to heat, Λ) (McKinley, 1961). The cross-sectional area ($S = \pi r^2$) and mass ($m = 4\pi\rho r^3/3$) can be related through r, to produce the following relation for any shape:

$$S = A_\mathrm{s}\left(\frac{m}{\rho}\right)^{\frac{2}{3}}. \tag{1}$$

As the meteoroid moves through the atmosphere, it sweeps a volume of air equivalent to a cylinder with volume $Sv\mathrm{d}t$. The mass of this volume is $\mathrm{d}m_\mathrm{a} = \rho_\mathrm{a} Sv\mathrm{d}t$, and inserting S from Equation (1) into this expression leads to an equation for the rate of changing air mass encountered by the meteoroid (McKinley, 1961):

$$\mathrm{d}m_\mathrm{a} = \rho_\mathrm{a}\left(\frac{m}{\rho}\right)^{\frac{2}{3}} A_\mathrm{s} v\mathrm{d}t. \tag{2}$$

The rate of change of momentum of the meteoroid is

$$\frac{\mathrm{d}(mv)}{\mathrm{d}t} = v\frac{\mathrm{d}m}{\mathrm{d}t} + m\frac{\mathrm{d}v}{\mathrm{d}t}. \tag{3}$$

Thus, the air particles in this volume will gain momentum per unit time, which can be expressed as

$$\Gamma\frac{\mathrm{d}m_\mathrm{a}}{\mathrm{d}t}v = \Gamma A_\mathrm{s}\left(\frac{m}{\rho}\right)^{\frac{2}{3}}\rho_\mathrm{a} v^2. \tag{4}$$

The first term on the right-hand side in Equation (3), $v(\mathrm{d}m/\mathrm{d}t)$, can be ignored, since it is assumed to be negligible for small meteoroids ($m \gg \mathrm{d}m$). Equating the

remaining term in Equation (3), $m(\mathrm{d}v/\mathrm{d}t)$, with the momentum gained by the air particles yields as exhibited in Equation (4) results in the drag equation:

$$\frac{\mathrm{d}v}{\mathrm{d}t} = -\frac{\Gamma A_\mathrm{s}\rho_\mathrm{a}v^2}{m^{1/3}\rho^{2/3}}\,. \tag{5}$$

The negative sign in Equation (5) indicates deceleration. Considering that the rate of mass loss is proportional to the kinetic energy, it can be written in terms of the differential mass equation (McKinley, 1961), also known as the mass-loss equation (Ceplecha et al., 1998):

$$\frac{\mathrm{d}m}{\mathrm{d}t} = -\frac{\Lambda A_\mathrm{s}\rho_\mathrm{a}v^3m^{2/3}}{2\xi\rho^{2/3}}\,. \tag{6}$$

The absolute visual meteor magnitude (M_v) is expressed in terms of the luminous power I (in units of watts). Luminous power is a portion of the total radiation in the visual bandpass (400–700 nm), with a peak sensitivity at about 560 nm. According to Öpik (1958),

$$M_\mathrm{v} = 6.8 - 2.5\log_{10} I. \tag{7}$$

In principle, the absolute magnitude M_v is defined as the magnitude the meteor would have if it were placed in the zenith at a height of 100 km (McKinley, 1961). While Equation (7) suggests that a meteor with $M_\mathrm{v} = 0$ should radiate visible light at a rate of 525 W, it should be noted that I depends on the spectral energy distribution of the meteor. We have

$$I = -\tau_I\frac{\mathrm{d}E_\mathrm{kin}}{\mathrm{d}t} = \tau_I\left(\frac{v^2}{2}\frac{\mathrm{d}m}{\mathrm{d}t} + mv\frac{\mathrm{d}v}{\mathrm{d}t}\right), \tag{8}$$

where τ_I is the velocity-dependent dimensionless luminous efficiency factor (Öpik, 1958) and E_kin is the kinetic energy of the meteoroid. For meteoroids with $v_\infty > 16$ km/s, deceleration is negligible (Ceplecha et al., 1998), and thus the term $mv(\mathrm{d}v/\mathrm{d}t)$ is usually ignored. Generally, it is assumed that the light produced by meteors (in a specific bandpass) is proportional to the meteoroid mass loss rate. Thus, a "photometric" mass of the meteoroid could be estimated by integrating Equation (8) over the length of the entire light curve. The summary of the methodologies used to infer the mass of the meteoroid can be found in Silber (2014) and Silber et al. (2015). The smallest meteoroids capable of producing shock waves strong enough to generate infrasound signatures detectable at the ground are within the centimeter-size range. A more detailed discussion about the formation of meteor-generated shock waves is given in Silber et al. (2017).

3 Infrasound

3.1 What is infrasound?

Sound is a pressure (or longitudinal) wave. The part of the acoustic spectrum associated with meteoroid propagation through the atmosphere is known as infrasound, extending from just below the threshold of human hearing down to the natural oscillation of the atmosphere. For comparison, human hearing lies between approximately 20 Hz and 20 kHz (Figure 2).

Figure 2 – The sound frequency spectrum.

The speed of sound depends on the thermal structure (Figure 3) of the atmosphere. At sea level, the speed of sound in air at 20° C is 343 m/s. Infrasound waves attenuate due to spreading losses and absorption (Sutherland and Bass, 2004). Higher frequencies (e.g., audible sound) attenuate very quickly. Low frequency waves however, can propagate over very long distances, making infrasound an excellent tool for studying distant explosive sources in the atmosphere (e.g., Christie and Campus, 2010).

As a dynamic and continuously changing medium, the atmosphere can significantly and often irreversibly affect the propagation of infrasound waves. Seasonal variations, winds, temperature inversions, turbulence, and gravity waves are only some of the factors that can adversely affect infrasound. An example illustrating a seasonal wind variation in the mid-northern latitudes is shown in Figure 4. A depiction of an idealized waveform is illustrated in Figure 5, (a). Due to Doppler shifting, the signal period might get either compressed (upwind propagation) or stretched (downwind propagation), as shown in Figure 5, (b). The signal amplitude is also susceptible to winds, whereby downwind propagation increases the amplitude, and upwind propagation suppresses it (e.g., Silber et al., 2015).

Although the instantaneous changes might be minute, they are cumulative and could have significant contribution by the time the signal reaches the station, especially for a wave propagating over long distances.

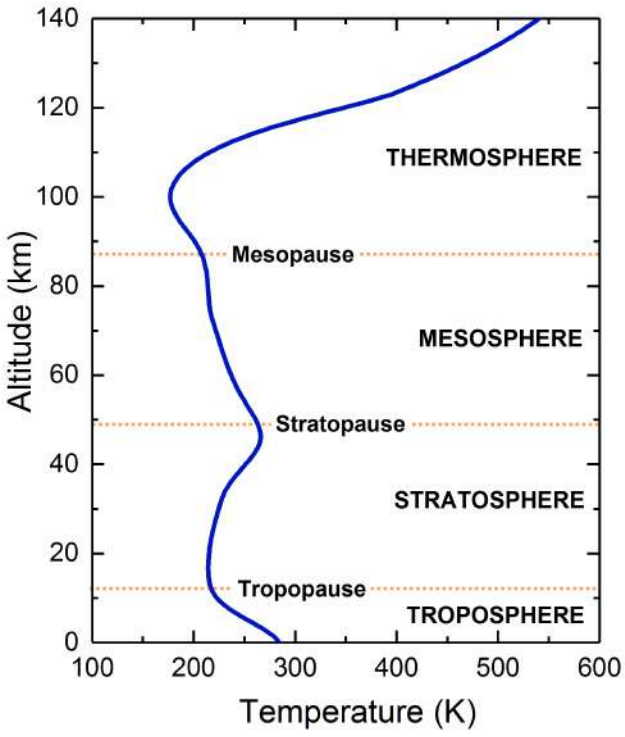

Figure 3 – Thermal structure of the atmosphere.

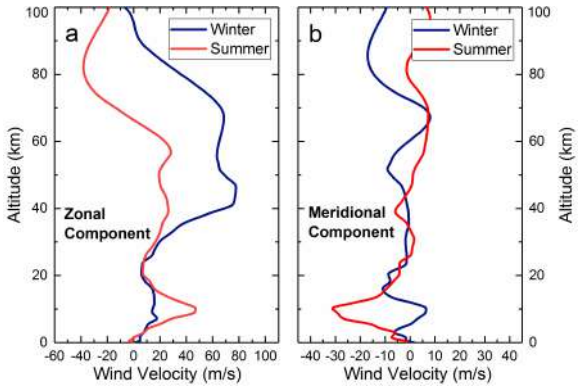

Figure 4 – Examples of the (a) zonal (east-west) and (b) meridional (north-south) components of the wind velocity vector for mid-northern latitudes in summer and winter up to 100 km altitude. Note that the scale along the x-axis is not the same in panels (a) and (b).

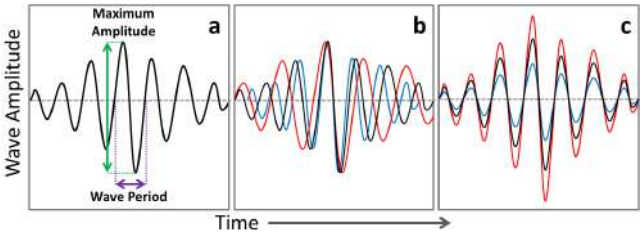

Figure 5 – Panel (a) shows an idealized waveform with a signal at the center (denoted by the maximum amplitude). The wave period is also shown. In panels (b) and (c), the waveform drawn with black line represents the original signal before it is affected by the propagation effects due to winds. The superimposed red and blue waveforms show the appearance of the signal after it is affected by the propagation: stretched wave period (downwind) and compressed wave period (upwind) in panel (b); increased amplitude (downwind) and suppressed amplitude (upwind) in panel (c).

Additionally, infrasound sound waves in the atmosphere reflect and refract, and can take various propagation paths (affected by density and temperature stratification in the atmosphere, as well as the winds), known as waveguides, as illustrated in Figure 6.

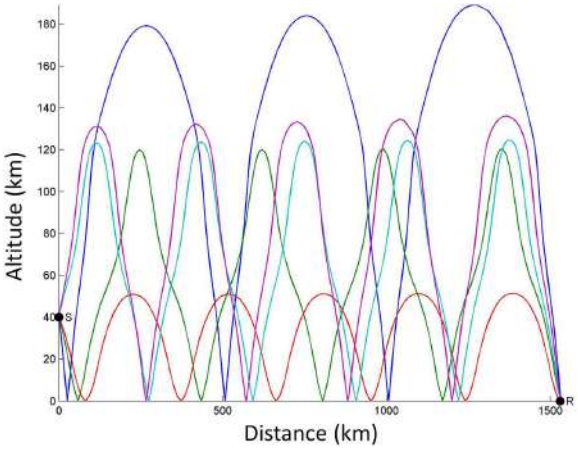

Figure 6 – Representative infrasonic ray paths emanating from a source (S) located at 40 km altitude. The receiver (R) is located on the ground level, at horizontal distance of 1500 km from the source. Various ray paths are shown. The rays coming straight down from the source to the ground (at the distance of up to ca. 100 km in the scenario shown) before reflecting back up are called direct arrivals.

There are many sources of infrasound, both man-made and natural. Some examples of man-made sources are mining activities and explosions. Examples of natural sources are lightning, earthquakes, and meteors. The wave period and frequency of many of these sources overlap (Figure 7), often making identification and characterization of the source a daunting task.

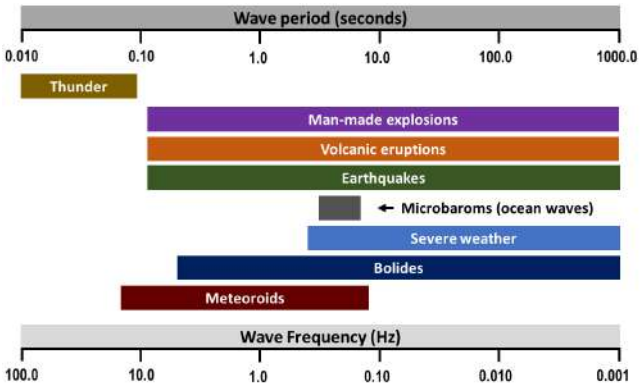

Figure 7 – Infrasound wave periods for some typical sources. Meteors can produce infrasound within the period and frequency range of other sources, making the identification process challenging.

3.2 Historical considerations

The first instrumentally recorded infrasound dates back to 1883, when a violent volcanic eruption nearly wiped out the entire island of Krakatoa, Indonesia (Verbeek, 1884). Infrasound waves circled the globe several times (Abercromby et al., 1888).

The first documented infrasonic records from a meteoritic event came from the well-known Tunguska event that took place on 30 June 1908. The blast wave released by this event was so intense that it generated low frequency acoustic waves recorded by microbarographs in England. The recordings of the Tunguska event, as originally published by Whipple (1930), are shown in Figure 8.

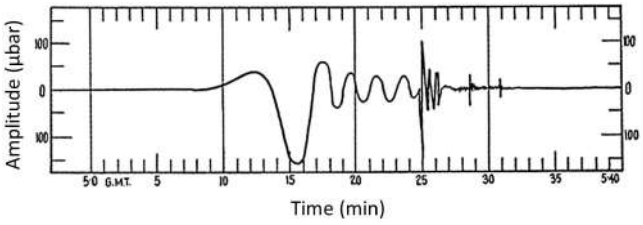

Figure 8 – Infrasound pressure wave from the Tunguska explosion recorded in the UK (Whipple, 1930).

Infrasound was used primarily in the military domain during the Cold War era for the purpose of detecting nuclear explosions. The United States Air Force Technical Applications Center (AFTAC) had arrays installed all over the globe (Cook and Bedard, 1972; ReVelle, 1997; Silber et al, 2009). During that period, the measurements of signal amplitude and period from nuclear explosions were used to develop empirical relations to estimate the amount of energy released. This point will be discussed in more detail in Section 4.3.

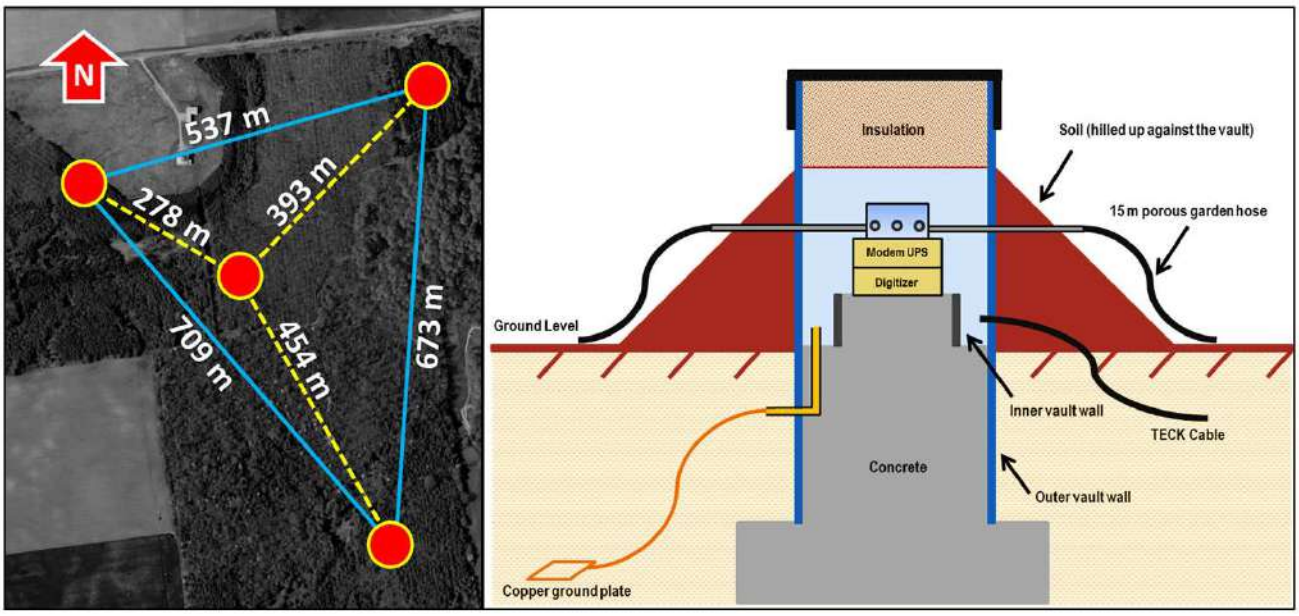

Figure 9 – Left: The planar configuration of the infrasound array at the Elgin Field Infrasound Array (ELFO) near London, Ontario, Canada (gound map credit: Google Earth). *Right*: The vault housing the infrasound array element at ELFO. The sensor is stacked on top of the modem and digitizer.

After the Cold War ended, infrasound fell into obscurity. It was not until the inception of the Comprehensive Test-Ban Treaty Organization (CTBTO) in Vienna in the early 1990s that infrasound experienced a renaissance. The CTBTO network employs four methodologies to monitor and detect illicit explosions around the globe; these are seismic, hydroacoustic, radio nuclide, and infrasound. The Infrasound Monitoring System (IMS) consists of 60 stations distributed around the globe with the aim to provide enough coverage to detect a one kiloton of TNT equivalent (which corresponds to an energy of 4.184×10^{12} J) explosion anywhere (Christie and Campus, 2010). As of early 2018, 49 stations are fully certified and in operation, and the remaining 11 are either installed or planned. The data from all these stations is sent to the International Data Center (IDC) in Vienna, Austria (Christie and Campus, 2010) for further analyses. Scientists are also using infrasound recorded at these stations to study signals produced from a plethora of other sources, both natural and anthropogenic (e.g., lightning, volcanoes, surf, meteors, and mining), and develop new and validate existing propagation models.

3.3 Infrasound arrays

A typical infrasound array is comprised of four or more sensors (also called array elements) in a planar arrangement, as shown in Figure 9. In essence, an infrasound sensor is an extremely sensitive microphone that can detect minute changes in the ambient air pressure (Figure 10). The sensors are usually housed in insulated concrete vaults and protected from the elements, as illustrated in Figure 9. The data are sampled at 20 or more samples per second, and then digitized and stored on a server for further signal processing. As the airwave sweeps across the array, each sensor receives the signal at a slightly different time. Through array processing techniques, the difference in signal arrival times at each sensor provides the direction of arrival (back azimuth) of coherent plane waves. The apparent horizontal velocity (trace velocity) provides information about the coherence or correlation of the signal energy. Since the winds are the major source of the noise at the ground, pipes or porous hoses are used to reduce the local noise (Figure 9). Natural ground cover, such as vegetation, can also serve as a means of filtering the local noise.

There is a dedicated infrasound array for observations of meteors near London, Ontario, Canada, operating alongside the All-Sky Camera Network. The array elements are positioned such that the array is optimized for 1 Hz peak frequency detection. An overview of the Elgin Field Infrasound Array (ELFO) setup is given in Silber (2014) and the Supplemental Material of Silber and Brown (2014).

Figure 10 – Infrasound sensor. The unit shown here is Chaparral 25, produced by Chaparral Physics, Alaska, USA. The unit is approximately 25 cm in diameter. Image credit: `http://www.chaparralphysics.com`.

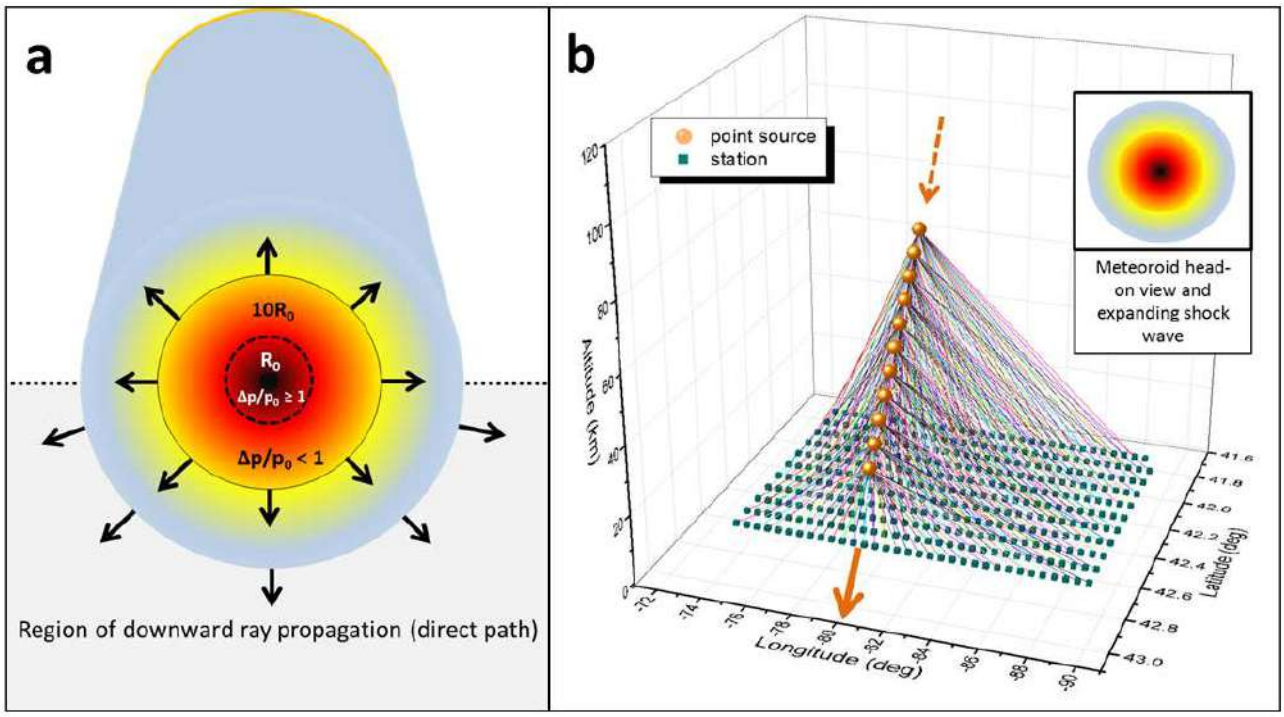

Figure 11 – The diagram in panel (a) shows the cylindrical line source generated by a meteoroid travelling out of the page. The highly nonlinear strong shock region is denoted by R_0. The shock wave expands radially outward. The horizontal dotted line separates the region of downward and upward ray propagation. The diagram in panel (b) shows downward propagating rays from the hypersonic line source. For better visualization, the rays are shown as being generated by discrete points, but, in reality, the shock wave is generated continuously along the propagation path.

4 Detecting meteors with infrasound

4.1 Meteors as sources of infrasound

As mentioned in the Introduction, a meteoroid can generate shock waves in two ways: (1) during its hypersonic passage through the atmosphere (hypersonic line source); and (2) when it undergoes gross fragmentation, typically towards the end of it trajectory (point or quasi-spherical source) (Figure 1). Upon the formation of the shock wave, highly non-linear processes take place in the physical region immediately behind the shock front, and where the overpressure (pressure of the shock front relative to the pressure of the ambient air) satisfies $\Delta p/p_0 \geq 1$. This region, also called the characteristic or blast radius (R_0), delineates the space of maximum energy deposition. The shock wave, as it propagates outward, loses energy to the surrounding atmosphere, and, after it has traveled a distance around $10R_0$, decays into a weak shock regime (the overpressure drops to below 1). This is illustrated in Figure 11, (a), for a meteoroid generating a hypersonic line source during its propagation through the atmosphere.

Conceptually, the blast radius can be thought of as the radius of the cylindrical volume that could be generated if all of the explosion energy was used in performing work on the surrounding atmosphere at ambient pressure (p_0). The mathematical expression for R_0 is

$$R_0 = \left(\frac{E_0}{p_0}\right)^{\frac{1}{2}}, \tag{9}$$

where E_0 is the energy released by the meteoroid per unit length (e.g., Tsikulin, 1970). For the purely hypersonic motion (i.e., no fragmentation episodes), R_0 can be approximated in terms of the meteoroid diameter (d_m) and Mach number (M):

$$R_0 \approx M d_\mathrm{m}. \tag{10}$$

Equation (10) tells us that larger and faster (more energetic) meteoroids will produce a larger blast radius than the meteoroids that are small and relatively slow. This is exactly what Equation (9) implies—the size of the blast radius is directly proportional to (the square root of) the amount of energy released by the meteoroid. Beyond approximately $10R_0$, the wave is considered to be in the weak shock regime. We can relate the blast radius to the fundamental period (τ_0) of the wave through the following expression:

$$\tau_0 = \frac{2.81 R_0}{c_0}, \tag{11}$$

where c_0 is the local speed of sound. The wave period and frequency are inversely proportional and therefore the fundamental frequency of the wave is $f_0 = 1/\tau_0$. This means that an energetic source which generates a large blast radius will have a long fundamental wave period and thus a low fundamental frequency. Since low frequencies attenuate much more slowly than high frequencies (see Section 3.1), infrasound from energetic sources can travel over very long distances (hundreds to tens of thousands of kilometers). This is what makes infrasound an excellent monitoring tool. Due to nonlinear effects, the wave period will lengthen with the distance (e.g., Landau, 1945; DuMond et al., 1946). Additionally, during propagation, the weak shock might decay

into a linear acoustic wave, and, if it does, the wave period will undergo further alterations. Since further details and discussion on this topic are well beyond the scope of the present paper, the reader is directed to the following sources: ReVelle (1974), Edwards (2010), Silber (2014), Silber et al. (2015) and Silber and Brown (2019).

4.2 Near-field and far-field infrasound

The cylindrical shock generated by a meteoroid propagates outward in all directions, as depicted in Figure 11, (a). Given favorable atmospheric conditions, the downward propagating rays could reach the receiver on the ground (see Figure 6). Such airwaves produce so-called direct arrivals or near-field infrasound. In physical terms, direct arrivals are possible up to approximately 250 km from the source (Figure 6). Despite the relatively short distance, even direct arrivals could suffer from propagation effects due to the winds and other atmospheric conditions (see Silber and Brown, 2014). A 3D-diagram in Figure 11, (b), depicts idealized direct-arrival infrasonic rays emanating from a meteor. For clarity, the rays are shown as being generated by discrete points, although, in reality, the shock wave is generated continuously along the propagation path. An infrasound station (receiver) located at any point depicted by a small square on the ground will receive the signal that corresponds to the energy deposition at a specific point along the propagation path. Thus, only a "snapshot" of the entire line source will be captured at a given station, and the signal attributes, such as the period and amplitude, will be representative of the shock conditions at that particular point. The situation is further complicated if the meteoroid is undergoing strong ablation and/or fragmentation episodes. Additionally, the propagation effects (e.g., attenuation, absorption, winds, turbulence) will inevitably modify the airwave before it arrives at the station. To visualize this, we can take a look at the meteor event in Figure 11, (b). The signal emanating from the altitude of 80 km will not be identical to the signal coming from other altitudes, for example, 60 km or 40 km, even though they are all generated by the same meteoroid. If there is gross fragmentation at 30 km altitude, a signal arriving from higher altitudes will not reflect that.

Far-field infrasonic rays may take various propagation paths, as shown in Figure 6, and are more susceptible to propagation effects before reaching the receiver. In far-field infrasound, it is common to approximate the line source as a point source, because the length of the trajectory is much smaller than the distance between the source and the receiver (ReVelle, 1976). Given large propagation distances, it becomes increasingly more difficult, if not impossible, to determine the altitude from which the signal originates (Silber et al., 2011).

4.3 Energy estimates

There are numerous empirical yield relations that can be employed to estimate the energy of an explosive source. Most of these were developed for the purpose of estimating the energy produced by nuclear explosions (see, e.g., Ens et al., 2012, and references therein). Some empirical relations are based on the combination of signal amplitude and distance between the source and the receiver, while others are based on the signal period alone. The signal period (τ) offers a more robust means of estimating the energy release as opposed to the signal amplitude. This is because the amplitude is much more susceptible to propagation effects, leading to energy estimates that could vary by an order of magnitude (e.g., Ens et al., 2012).

The empirical period-yield relations developed by AFTAC during the Cold War to estimate the energy released by nuclear explosions were adapted for bolides by ReVelle (1997). In these relations, the signal period represents the full cycle measurement at the maximum amplitude; see Figure 5, (a). About half of the total energy released by a nuclear explosion goes into radiation, hence the energy in Equations (12) below is divided by a factor of 2:

$$\begin{cases} \log_{10}\frac{E}{2} = 3.34\log_{10}\tau - 2.58 & (\frac{E}{2} \le 100 \text{ kT}); \\ \log_{10}\frac{E}{2} = 4.14\log_{10}\tau - 3.61 & (\frac{E}{2} > 40 \text{ kT}). \end{cases} \tag{12}$$

In Equations (12), τ is in seconds. It should be noted that the signal period from a nuclear explosion as recorded by various stations is usually stable, meaning that it does not vary much from station to station. In nuclear explosions, the source is stationary and the explosion more or less isotropic; therefore, the resulting signal periods are self-consistent. The opposite is generally true for meteors. In most events, the signal period varies from station to station, making energy estimates more problematic (e.g., Silber et al., 2009; 2011). These apparent differences are most likely associated with signals coming from different parts of the trail. Technically, only "snapshots" of the airwave (e.g., high latitude, low altitude, cylindrical line source, fragmentation events) will have favorable propagation paths reaching any given station. Nevertheless, the empirical period-yield relations still provide a robust estimate of energy release by bolides (e.g., Silber et al., 2009, 2011; Brown et al., 2013). The list of most commonly used empirical yield relations can be found in Silber and Brown (2019).

4.4 Observations of bright meteors

We now turn our attention to detections of meteors on a regional scale. Infrasound, while extremely useful in detecting impulsive sources in the atmosphere, should be combined with other techniques to establish ground truth and appropriately identify and characterize the source. For example, the airwave periods (and frequencies) produced by meteors are rather broad (Figure 7), and the signal appearance might be consistent with other sources such as lightning, aircraft sonic boom, mining, man-made explosions, and machinery. Thus, infrasound signal alone might not be sufficient to determine the type of source and/or derive meaningful information about that source. The best approach in setting up an infrasound station for detection of meteors is to place it within or close (less than 100 km)

to an existing all-sky camera network, such that direct arrivals can be received at the array. One such configuration has been in place since the early 2000s at Western University in Canada (the Elgin Field Infrasound Array, or ELFO), where radar, optical, VLF, and infrasound technologies are combined to provide simultaneous observations of meteor events (e.g., Weryk et al., 2007; Silber, 2013).

Early attempts to capture infrasound from simultaneously observed meteors were largely unsuccessful (for details, see Edwards, 2010). It was not until the inception of ELFO in 2006 that simultaneously observed events started to trickle in. About one meteor per month had been detected by both optical systems and infrasound (Edwards et al., 2008), with the database growing to nearly 80 events by 2011 (Silber, 2014; Silber and Brown, 2014). The factors adversely affecting the detection efficiency at ELFO are the predominantly cloudy weather in winter months (diminishing the capability to optically observe meteors), and infrasound noise emanating from the Niagara Falls during the summer months (stifling signal detection).

The detailed description of the method used to search for infrasound signals produced by meteors is outlined in Silber (2014) and Silber and Brown (2014). Consequently, only a brief summary is given here. First, it is necessary to obtain meteor parameters from optical observations (e.g., timing and beginning and end points of the meteor luminous path). Next, before searching for possible signals, one should determine the theoretical time window and direction of signal arrivals based on the parameters determined in the previous step (timing of the meteor, and the beginning and end points). The search for infrasound signals is done by employing a signal processing software package. The details on how this can be achieved most effectively are provided in Silber (2014) and Silber and Brown (2014). If a signal is found, then the event is flagged as positive and stored in a database for further processing. The latter will depend on what scientific goals are to be achieved. By combining infrasound with high-fidelity optical observations, a plethora of useful information about meteoroids can be established. Investigation of the detection efficiency, flux, energy estimates, improving propagation models, extracting the altitude at which shock was generated, are only a few examples of the many avenues one could explore.

As of early 2018, the database of 71 infrasound producing meteors detected on a regional scale compiled and analyzed by Silber and Brown (2014) remains the only such database globally.

5 Future work

Installations of infrasound arrays alongside existing all-sky camera networks would open new pathways in building up a large database of bright meteors generating infrasound on a regional scale and exploring interesting questions in meteor science. Data collected at different locations around the world can be amalgamated into a single database, which would provide a basis for better statistical analyses and building up a comprehensive picture about these events. Combining high-fidelity astrometric and photometric observations of meteors with infrasound records can provide ground truth information and provide important constraints that would be otherwise impossible to obtain. Some of the topics that could be explored in the future are the following:

- statistical analyses of meteoroids capable of producing infrasound detectable on the ground;
- signal characteristics of meteors producing infrasound on regional scale (e.g., frequency, period, amplitude, and morphology, and whether these can be used to infer information about the meteoroid);
- energy estimates for small (centimeter- to decimeter-sized) meteoroids and whether these scale the same way as large bolides;
- determination of shock altitudes as well as types of shockwave generated (cylindrical line source or spherical due to fragmentation);
- determination of meteoroid masses through infrasound observations of meteors;
- detection efficiency for infrasound installations;
- dedicated observations of meteor showers and how different meteor parameters might be reflected in infrasound signals and detection efficiency; and
- applications extending beyond the field of meteor science, such as validation and improvement of propagation models, which is especially important for global monitoring of illicit explosions (e.g., for CTBTO).

References

Abercromby R., Archibald E. D., Bonney T. G., Evans F. J., Geikie A., Judd J. W., Lockyer J. N., Russell F. A. R., Scott R. H., Stokkes G. G., Strachey R. E., Symons G. J., and Wharton W. J. L. (1888). *The Eruption of Krakatoa, and Subsequent Phenomena*. Report of the Krakatoa Committee of the Royal Society of London, Trubner, London.

Bronsthen V. A. (1983). *Physics of Meteoric Phenomena*. D. Reidel, Dordrecht, the Netherlands.

Brown P. G., Assink J. D., Astiz L., Blaauw R., Boslough M. B., Borovička J., Brachet N., Brown D., Campbell-Brown M., Ceranna L., Cooke W., de Groot-Hedlin C., Drob D. P., Edwards W., Evers L. G., Garces M., Gill J., Hedlin M., Kingery A., Laske G., Le Pichon A., Mialle P., Moser D. E., Saffer A., Silber E., Smets P., Spalding R. E., Spurný P., Tagliaferri E., Uren D., Weryk R. J., Whitaker R., and Krzeminski Z. (2013). "A 500-kiloton airburst over Chelyabinsk and an enhanced hazard from small impactors". *Nature*, **503**, 238.

Brownlee D. E. (1985). "Cosmic dust-collection and research". *Annual Review of Earth and Planetary Sciences*, **13**, 147–173.

Campbell-Brown M. D. and Koschny D. (2004). "Model of the ablation of faint meteors". *Astronomy & Astrophysics*, **418**, 751–758.

Ceplecha Z., Borovička J., Elford W. G., ReVelle D. O., Hawkes R. L., Porubčan V., and Šimek M. (1998). "Meteor phenomena and bodies". *Space Science Reviews*, **84**, 327–471.

Christie D. R. and Campus P. (2010). "The IMS infrasound network: design and establishment of infrasound stations". In Le Pichon A., Blanc E., and Hauchecorne A., editors, *Infrasound Monitoring for Atmospheric Studies*, pages 29–75. Springer.

Cook R. K. and Bedard, Jr. A. J. (1972). "On the measurement of infrasound". *Q. J. Royal Astron. Soc.*, **67**, 5–11.

DuMond J. W., Cohen E. R., Panofsky W. K. H., and Deeds E. (1946). "A determination of the wave forms and laws of propagation and dissipation of ballistic shock waves". *The Journal of the Acoustical Society of America*, **18**, 97–118.

Edwards W. N. (2010). "Meteor generated infrasound: theory and observation". In Le Pichon A., Blanc E., and Hauchecorne A., editors, *Infrasound Monitoring for Atmospheric Studies*, chapter 12, pages 361–414. Springer.

Edwards W. N., Brown P. G., Weryk R. J., and ReVelle D. O. (2008). "Infrasonic observations of meteoroids: Preliminary results from a coordinated optical-radar-infrasound observing campaign". *Earth, Moon, and Planets*, **102**, 221–229.

Ens T. A., Brown P. G., Edwards W. N., and Silber E. A. (2012). "Infrasound production by bolides: A global statistical study". *Journal of Atmospheric and Solar-Terrestrial Physics*, **80**, 208–229.

Keay C. S. (1980). "Anomalous sounds from the entry of meteor fireballs". *Science*, **210 (4465)**, 11–15.

Landau L. D. (1945). "On shock waves at a large distance from the place of their origin". *Sov. J. Phys.*, **9**, 496–500.

McKinley D. W. R. (1961). *Meteor Science and Engineering*. McGraw-Hill, New York.

Öpik E. J. (1958). *Physics of Meteor Flight in the Atmosphere*. Interscience Publishers, New York.

Popova O. (2005). "Meteoroid ablation models". *Earth, Moon, and Planets*, **95**, 303–319.

Popova O. P., Sidneva S. N., Strelkov A. S., and Shuvalov V. V. (2001). "Formation of disturbed area around fast meteor body". In Warmbein B., editor, *Proceedings of the Meteoroids 2001 Conference*, Kiruna, Sweden, 6–10 August 2001. pages 237–245. ESA SP-495.

ReVelle D. O. (1974). *Acoustics of Meteors—Effects of the Atmospheric Temperature and Wind Structure on the Sounds Produced by Meteors*. PhD thesis, Michigan Univ., Ann Arbor, MI, USA.

ReVelle D. O. (1976). "On meteorâĂŘgenerated infrasound". *Journal of Geophysical Research*, **81**, 1217–1230.

ReVelle D. O. (1997). "Historical detection of atmospheric impacts by large bolides using acoustic-gravity waves". *Annals of the New York Academy of Sciences*, **822**, 284–302.

Silber E. A. (2013). "Infrasound as a scientific tool to study meteors". In Gyssens M., Roggemans P., and Żołądek P., editors, *Proceedings of the International Meteor Conference*, Poznań, Poland, 22–25 August 2013. IMO. pages 136–138.

Silber E. A. (2014). *Observational and Theoretical Investigation of Cylindrical Line Source Blast Theory Using Meteors*. PhD thesis, Dept. of Physics and Astronomy, Western University, London, Ontario, Canada. `https://ir.lib.uwo.ca/etd/2112/`.

Silber E. A. and Brown P. G. (2014). "Optical observations of meteors generating infrasound—I. Acoustic signal identification and phenomenology". *JASTP*, **119**, 116–128.

Silber E. A. and Brown P. G. (2019). "Infrasound monitoring as a tool to characterize impacting Near-Earth Objects (NEOs)". In Le Pichon A., Blanc E., and Hauchecorne A., editors, *Infrasound Monitoring for Atmospheric Studies. Challenges in Middle-atmosphere Dynamics and Societal Benefits*. Springer, second edition edition. (In press).

Silber E. A., Brown P. G., and Krzeminski Z. (2015). "Optical observations of meteors generating infrasound: weak shock theory and validation". *Journal of Geophysical Research: Planets*, **120**, 413–428.

Silber E. A., Hocking W. K., Niculescu M. L., Gritsevich M., and Silber R. E. (2017). "On shock waves and the role of hyperthermal chemistry in the early diffusion of overdense meteor trains". *Mon. Notices Royal Astron. Soc.*, **469**, 1869–1882.

Silber E. A., Le Pichon A., and Brown P. G. (2011). "Infrasonic detection of a near-Earth object impact over indonesia on 8 October 2009". *Geophysical Research Letters*, **38**, L12201.

Silber E. A., ReVelle D. O., Brown P. G., and Edwards W. N. (2009). "An estimate of the terrestrial influx of large meteoroids from infrasonic measurements". *Journal of Geophysical Research: Planets*, **114**, E08006.

Spalding R., Tencer J., Sweatt W., Conley B., Hogan R., Boslough M., Gonzales G., and Spurný P. (2017). "Photoacoustic sounds from meteors". *Scientific Reports*, **7**, 41251.

Sutherland L. C. and Bass H. E. (2004). "Atmospheric absorption in the atmosphere up to 160 km". *The Journal of the Acoustical Society of America*, **115**, 1012–1032.

Tsikulin M. A. (1970). *Shock Waves During the Movement of Large Meteorites in the Atmosphere*. Report No. NIC-Trans-3148. Naval Intelligence Command, Alexandria VA, USA, eTranslation Div.

Verbeek R. D. M. (1884). "The Krakatoa eruption". *Nature*, **30**, 10–15.

Weryk R. J., Brown P. G., Domokos A., Edwards W. N., Krzeminski Z., Nudds S. H., and Welch D. L. (2007). "The Southern Ontario all-sky meteor camera network". *Earth, Moon, and Planets*, **102**, 241–246.

Whipple F. J. W. (1930). "The great Siberian meteor and the waves, seismic and aerial, which it produced". *Q. J. Royal Meteorol. Soc.*, pages 278–304.

Wylie C. C. (1932). "Sounds from meteors". *Popular Astronomy*, **40**, 289.

Handling Editor: Marc Gyssens

First simultaneous radiometric and video observations of fireballs using a low-cost radiometer

Damir Šegon[1], *Denis Vida*[2,3], *Matej Butković*[4], *Mirjana Malarić*[5], *and Renato Turčinov*[6]

We give an update on the development of a low-cost meteor radiometer and present an improved design. We discuss light pollution noise removal techniques and outstanding problems. Finally, we present first simultaneous video and radiometric observations of fireballs with the system.

Received 2018 January 30

1 Introduction

Meteor radiometers are sensitive photometers capable of sampling the total brightness of the sky at very high sampling rates (> 100 samples per second). Since their introduction (Spurny et al., 2001), radiometers have proven to be invaluable in modelling fireball fragmentation (Borovička et al., 2015) as they have a much higher dynamic range than optical instruments and thus do not suffer from saturation effects, while capturing every minor variation in the light emitted from the fireball. For example, Spurny, Borovička, and Shrbeny (2006) noticed that some fireballs have interesting periodic light curves, while Spurny and Ceplecha (2008) described millisecond flares. Shrbeny and Spurny (2013) demonstrated that velocity of fireballs can be estimated from radiometric observations within a few km s^{-1} when optical dynamical data is not available. As radiometers can work even under overcast skies, and if one pairs the trajectory estimated from seismic data (Pujol et al., 2005; Kalenda et al., 2014) and velocity estimated from radiometers, orbits of fireballs can be calculated without the need for direct imaging. In that case, clear fragmentation needs to be present in the seismic data and it has to coincide with flares in the radiometric light curve.

Denis Vida et al. (2015) presented a low-cost version of a meteor radiometer which used one BPW34 photodiode and a single amplifier, but this configuration was not sensitive enough for detecting anything but the brightest fireballs. Damir Šegon et al. (2016) improved on the initial design by using three triples of photodiodes, summing and amplifying the signal from every triplet. Here we present first observational results with this system and compare them with video data.

2 Hardware setup

The radiometer system consists of nine BPW34 photodiodes which are grouped in three triplets. The diodes in the triplets are connected in parallel so their signals are effectively summed. The three summed signals are amplified using the LMC6464 quad amplifier, the three amplified signals are summed and again amplified using the fourth remaining channel of the amplifier.

The amplifier is battery powered by a 12 V battery to avoid introducing noise to the input signal. Initially we have used 9 V batteries, but their reliability and power output are strongly dependant on the quality of the battery and temperature, thus and we cannot recommend their usage. We recommend using 12 V UPS or car batteries as a more reliable source of power.

The amplified signal is sampled by an Arduino-based signal acquisition device (DAQ) which uses the AD7705 signal digitizer which is capable of sampling an analog signal at 500 samples per second with a 16-bit resolution. Detailed instructions how to build this data acquisition device are given in a guide available on the Instructables website[a]. The board with the photodiode array, the amplifier and the DAQ board are packed in a waterproof box and mounted on the roof of the Pula Observatory in Croatia, as shown in Figure 1. We estimate the cost of system to be around $75 USD. The planar configuration of photodiodes is not optimal for all-sky purposes as the diodes have an angle of half-sensitivity of $\pm 65°$, while at an elevation above horizon of 10° the sensitivity is only about 20%. More optimal configurations will be explored in the future. Nevertheless, if the coverage is dense enough, low-elevation sensitivity should not present any issues – we plan to have a network of radiometers in the near future.

The DAQ is connected via USB interface to a Raspberry Pi 2 single-board computer on which a Python script is running an acquisition thread and saving the data into 10 minute chunks. In practice we find the sample frequency to be a bit lower than 500 Hz, and is exactly 492.3683 Hz.

Hardware details, schematics, parts list are given in Appendix 6, while the Arduino and Python code is available on our Meteor Radiometer GitHub page[b]. In the near future we are planning to improve the DAQ board by implementing dynamic reference voltage scheduling – the background level can change during the night due to e.g. rising/setting of the Moon, which

[1]Astronomical Society Istra Pula, Park Monte Zaro 2, HR-52100 Pula, Croatia
[2]Department of Earth Sciences, University of Western Ontario, London, Ontario, N6A 5B7, Canada. Email: dvida@uwo.ca
[3]Department of Physics and Astronomy, University of Western Ontario, London, Ontario, N6A 3K7, Canada
[4]Grammar school "Gimnazija Pula", Trierska 8, HR-52100 Pula, Croatia
[5]Jelkovec High School, Vladimira Stahuljaka 1, HR-10360 Sesvete, Croatia
[6]Uljanik TESU elektronika d.o.o., Flaciusova 1, 52100 Pula, Croatia

IMO bibcode WGN-462-segon-radiometer
NASA-ADS bibcode 2018JIMO...46...62S

[a]Arduino 16-bit 500 SPS DAQ: https://www.instructables.com/id/Arduino-16-bit-500SPS-Dual-Channel-DAQ/ (Accessed January 9, 2018)

[b]CMN Meteor Radiometer: https://github.com/CroatianMeteorNetwork/MeteorRadiometer (Accessed January 9, 2018)

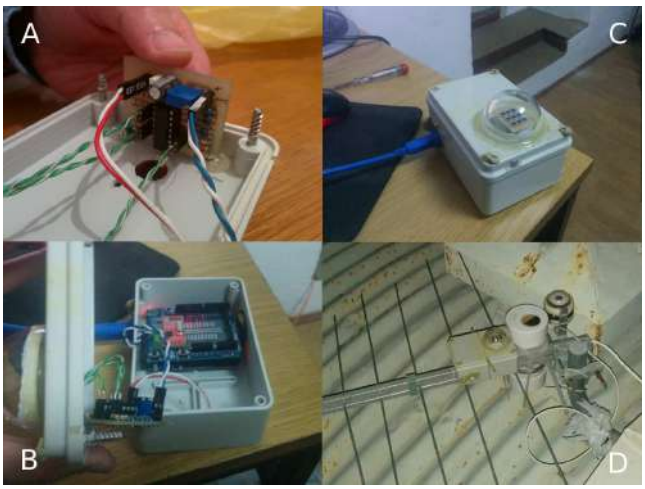

Figure 1 – Meteor radiometer hardware setup. A) Amplifier board with a 4 channel LMC6464 amplifier. Three triples of BPW34 photodiodes are connected to individual channels, their signals are amplified, summed, and amplified again through the fourth remaining channel. B) Amplifier board is packed in a box with an Arduino-based DAQ. C) Nine photodiodes are protected by an acrylic dome. D) The radiometer is mounted next to an SQM meter and an all-sky camera.

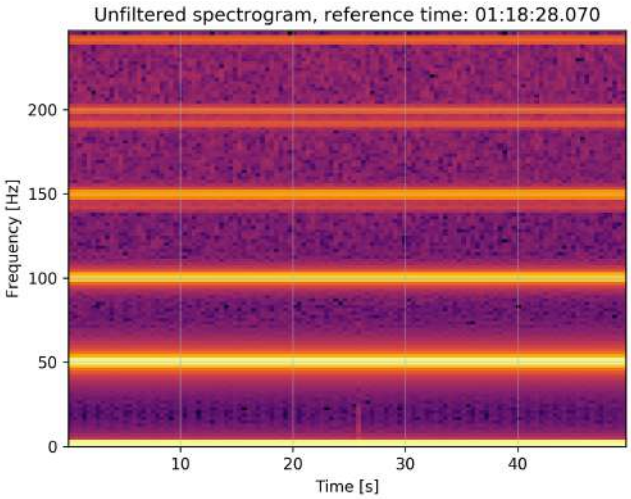

Figure 2 – Spectrogram of a 50 second sample from the radiometer taken on December 31, 2017. The fireball signature is visible around 26 s at lower frequencies.

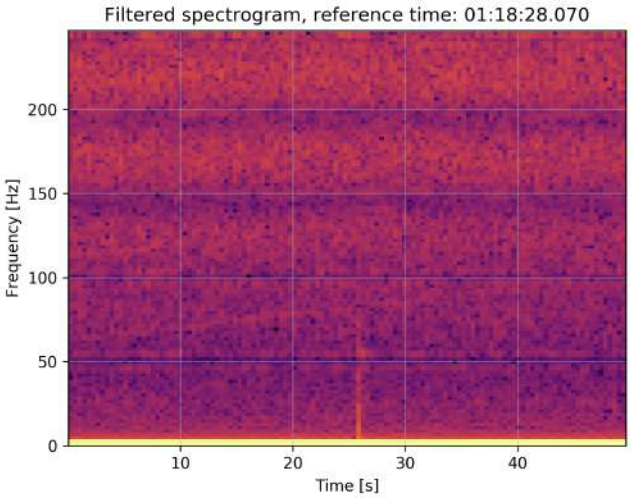

Figure 3 – Spectrogram of a 50 second filtered sample from the radiometer taken on December 31, 2017. The fireball signature is visible around 26 s at lower frequencies.

can reduce the dynamic range and make bright fireballs saturate. By having a dynamic reference voltage the system will always try to keep an optimal amount of the dynamic range above the background noise.

3 Noise filtering

As the radiometer is located in the light polluted city of Pula, we have given much effort to filtering the radiometric signal. We have found that the greatest contribution to the noise is made from walls that are reflecting lamplight and are in direct line of sight of the radiometer, thus care has to be taken to prevent sources of artificial lighting from reaching the sensor. Figure 2 shows the spectrogram of a 50 second sample of data from the radiometer. High presence of 50 Hz noise and its harmonics is visible which is caused by the light pollution. Furthermore, minor components can be noticed at 142.3683 Hz and 192.3683 Hz which are caused by aliasing of negative harmonics at −100 Hz and −50 Hz respectively. These can be avoided by introducing an anti-aliasing low-pass filter in front of the input signal which would limit input frequencies to 250 Hz, satisfying the sampling theorem and avoid aliasing caused by undersampling.

We have explored several approaches to noise filtering with varying levels of success: applying digital filters, signal averaging, and noise modelling. Type I Chebyshev filters of the 3^{rd} order (Williams & Taylor, 1995) seem to be the most robust way of removing frequency components caused by the light pollution – Table 1 lists the characteristics of the set of seven filters used to completely remove the light pollution noise with the minimum influence on the radiometric signal itself. We are performing detrending on the filtered signal by applying Savitzky–Golay smoothening and subtracting the result from the signal. The resulting filtered lightcurve of a fireball is discussed in the next section and it is given in Figure 5, while the filtered spectrogram is given in Figure 3. The standard deviation of the filtered background varies throughout the night and is around 6 ADU on average. We are also experimenting with more advanced noise filtering methods which we will publish in the future.

Table 1 – List of Chebyshev filter characteristics used to remove the light pollution noise.

Frequency (Hz)	Band (Hz)	Ripple in the bandpass (dB)
50.0	7.5	10
100.0	5.5	10
150.0	3.5	10
200.0	3.5	10
241.5	3.5	10
142.5	2.5	10
192.5	2.5	10

Using a moving average is also effective, but we have found this approach too simplistic, as it effectively acts as a low-pass filter. To completely eliminate the 50 Hz component one needs to average 10 samples which effectively defeats the purpose of the radiometer.

Finally, the cleanest way of filtering is to model the background noise as a sum of sines (one for every noise harmonic) and perform a fit on a sample of noise. Such experiments were conducted but we have found that this approach is sensitive even to the minor changes in the frequency of the power grid. The stochastic variations of less than ±0.01 Hz, which are always present in the power grid, can cause the noise model to easily mismatch the data and prevent correct filtering. We have used a linear frequency drift model with limited success. Nevertheless, we believe this approach warrants more research as it would provide the cleanest way of filtering if the drifts of frequency and phase could be properly estimated.

3.1 Results

Since 2017 November 29 and up until the middle of 2018 January we have recorded at least 9 simultaneous radiometric and optical events (those were the ones we noticed manually). Here we present details of a fireball recorded on 2017 December 31 by four cameras of the Croatian Meteor Network and the radiometer in Pula, and give 8 radiometric light curves of other fireballs as well. The December 31 fireball was fairly fast, with the initial velocity of $V_{init} = 65.9 \mathrm{km\,s^{-1}}$. The image of the fireball is shown in Figure 4. The peak visual magnitude of the event as seen from Pula was between -5^M and -6^M. Figure 5 shows the comparison between the radiometric and raw photometric light curves of the event – it can be seen that all cameras saturate soon after the beginning of the event, failing to capture the full range of fireball's intensity. This effect can somewhat be mitigated by applying a saturation correction, but such methods have certain limits (see Jenniskens et al. (2011), section 2.8 for further discussion).

From this event we estimate that the sensitivity threshold of our radiometer is about -2^M. The sensitivity can be greatly improved by moving the system under darker skies where gain can be increased and the light pollution noise would not be a large issue.

Figures 6 to 13 show side by side comparisons of coadded video frames of 8 fireballs and their radiometric light curves. Red arrows are aligned with the direction of the fireball. Video light curves are intentionally offset from the radiometric light curve for visualization purposes. Video and radiometric light curves are not normalized as in Figure 5, but are arbitrarily scaled. The "Image column sums" light curve was obtained by rotating the image to make the fireball horizontal and summing up pixel intensities by column using AstroImageJ software[c]. Note that the lightcurve of fireball on Figure 7 is fully recorded by the radiometer despite cloudy weather, while video detections only show the last part of the fireball.

[c]AstroImageJ: `http://www.astro.louisville.edu/software/astroimagej/` (Accessed January 29, 2018)

Figure 4 – 2017 December 31 fireball over western Croatia. Left – from Hum with a HIKVISION IP DS-2CD4020F CMOS camera and detected by the RMS software, courtesy of Aleksandar Merlak. Right – from Pula with an allsky camera visible on Figure 1, inset D.

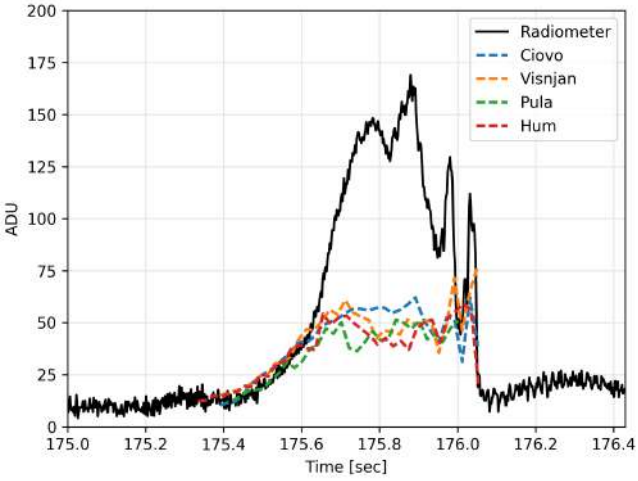

Figure 5 – Comparison of photometric and radiometric light curves of a 2017 December 31 fireball. The large dynamic range of the radiometer prevents saturation which significantly influences CCD photometry.

4 Conclusion

We have presented an updated design of a low-cost meteor radiometer and its first results. There are still outstanding issues with light pollution noise filtering, but a satisfactory solution was found by using Chebyshev filters. By comparing photometric light curves of fireballs with their radiometric counterpart, we find the sensitivity threshold of our radiometer design to be around -2^M under heavily light polluted skies, with possibility of improvement under darker skies. Furthermore, we find non-negligible saturation effects in video observations of fireballs which may have significant influence on photometric mass estimation.

5 Acknowledgements

We thank Peter Gural for reviewing the manuscript of this paper. We are also thankful to the Jelkovec High School for hosting an Arduino and radiometer workshop.

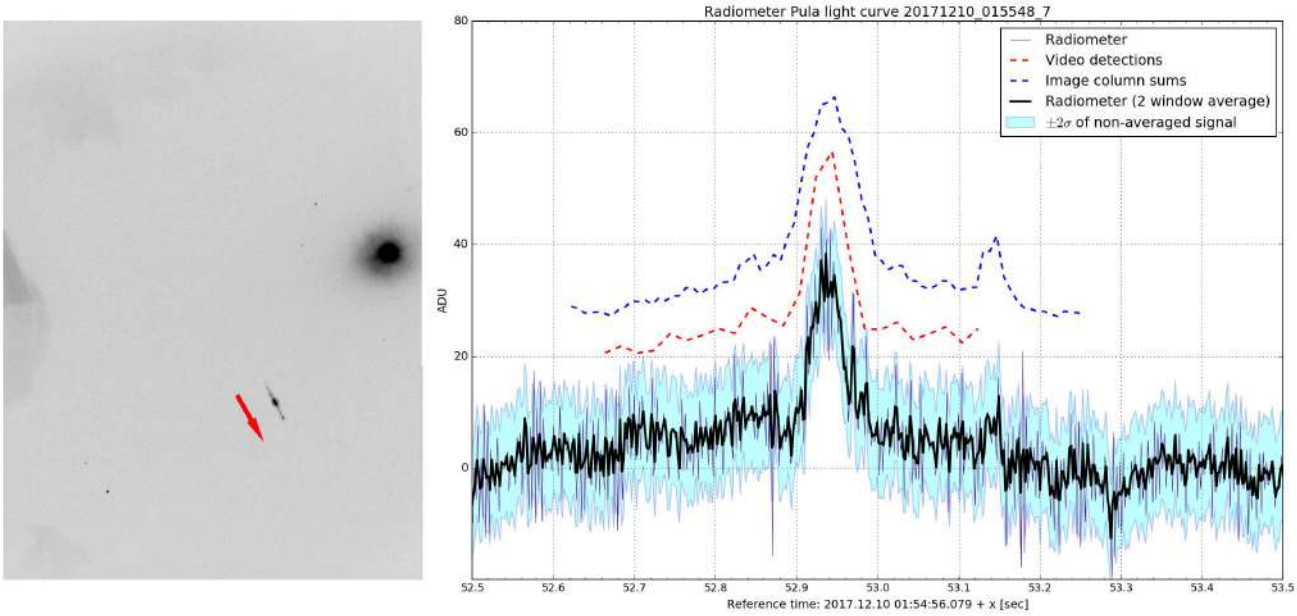

Figure 6 – 2017 December 10, $01^{h}55^{m}48^{s}$ fireball – video and radiometric lightcurve comparison.

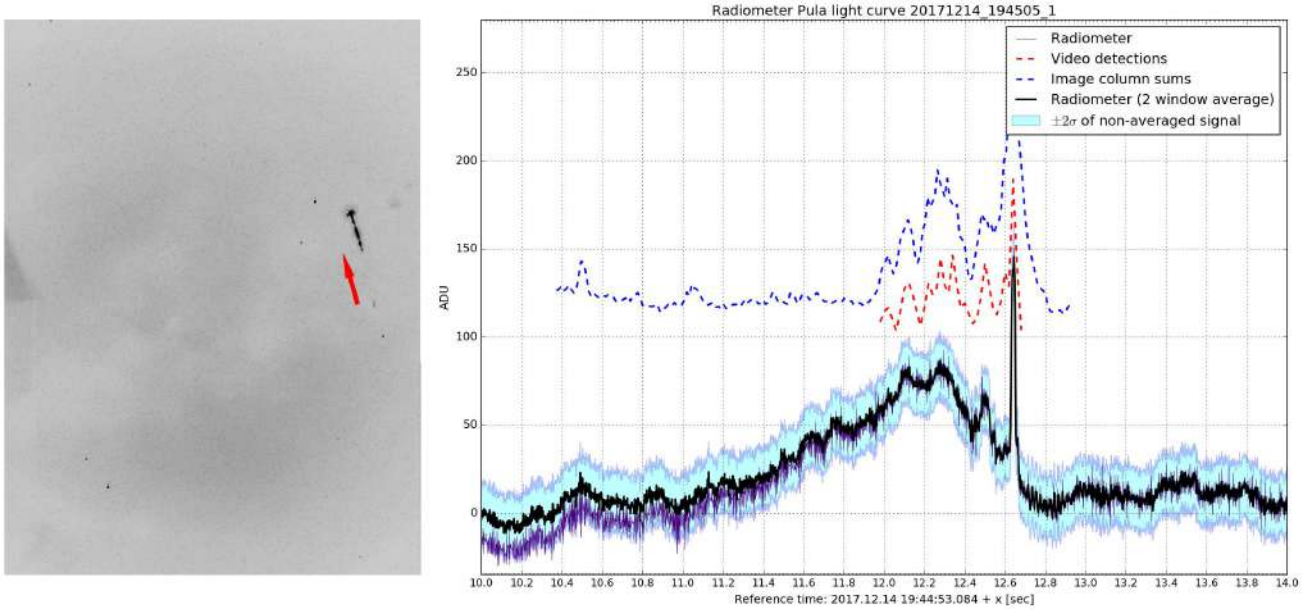

Figure 7 – 2017 December 14, $19^{h}45^{m}05^{s}$ fireball – video and radiometric lightcurve comparison. The fireball was recorded through patchy clouds.

6 Author Contributions

DŠ organized the project and developed the new version of the board with RT, DV wrote the article, improved the graphs and provided ideas for the project, MB conducted testing and improved data acquisition codes, and MM organized a radiometer workshop and conducted an interdisciplinary workshop on the importance of astronomy in engineering.

References

Borovička J., Spurny P., Šegon D., Andreić Ž., Kac J., Korlević K., Atanackov J., Kladnik G., Mucke H., Vida D., et al. (2015). "The instrumentally recorded fall of the Križevci meteorite, Croatia, February 4, 2011". *Meteoritics & Planetary Science*, **50:7**, 1244–1259.

Jenniskens P., Gural P., Dynneson L., Grigsby B., Newman K., Borden M., Koop M., and Holman D. (2011). "CAMS: Cameras for Allsky Meteor Surveillance to establish minor meteor showers". *Icarus*, **216:1**, 40–61.

Kalenda P., Borovička J., and Spurny P. (2014). "The localization of fireball trajectories with the help of seismic networks". *Studia Geophysica et Geodaetica*, **58:1**, 84–99.

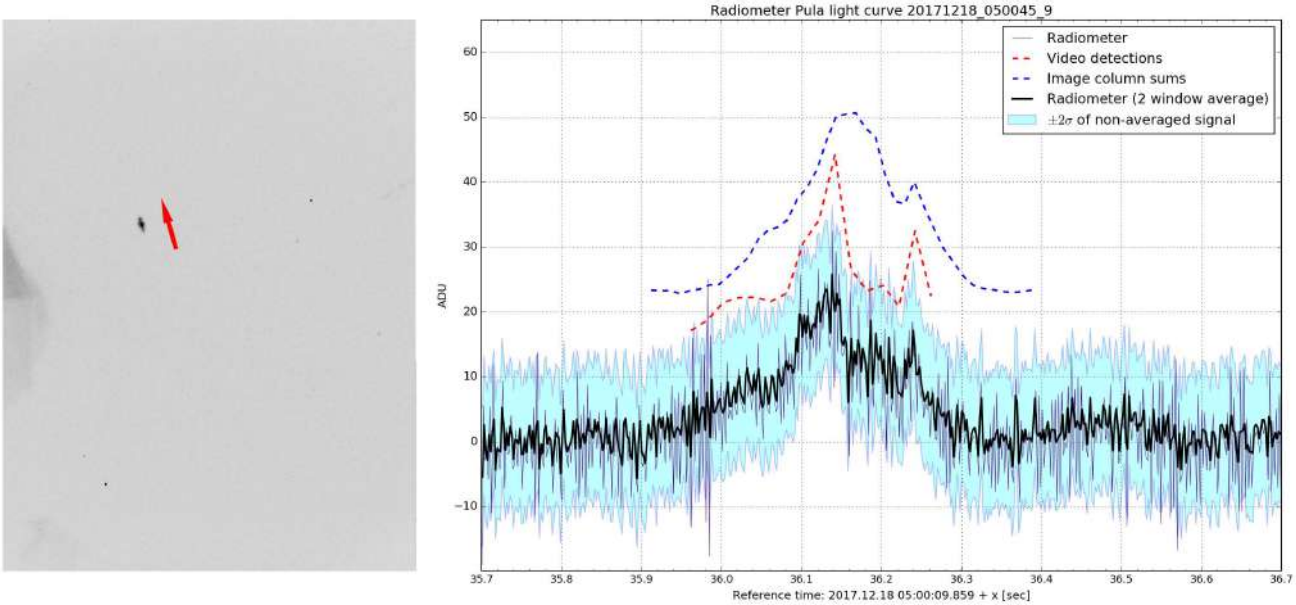

Figure 8 – 2017 December 18, $05^{h}00^{m}45^{s}$ fireball – video and radiometric lightcurve comparison.

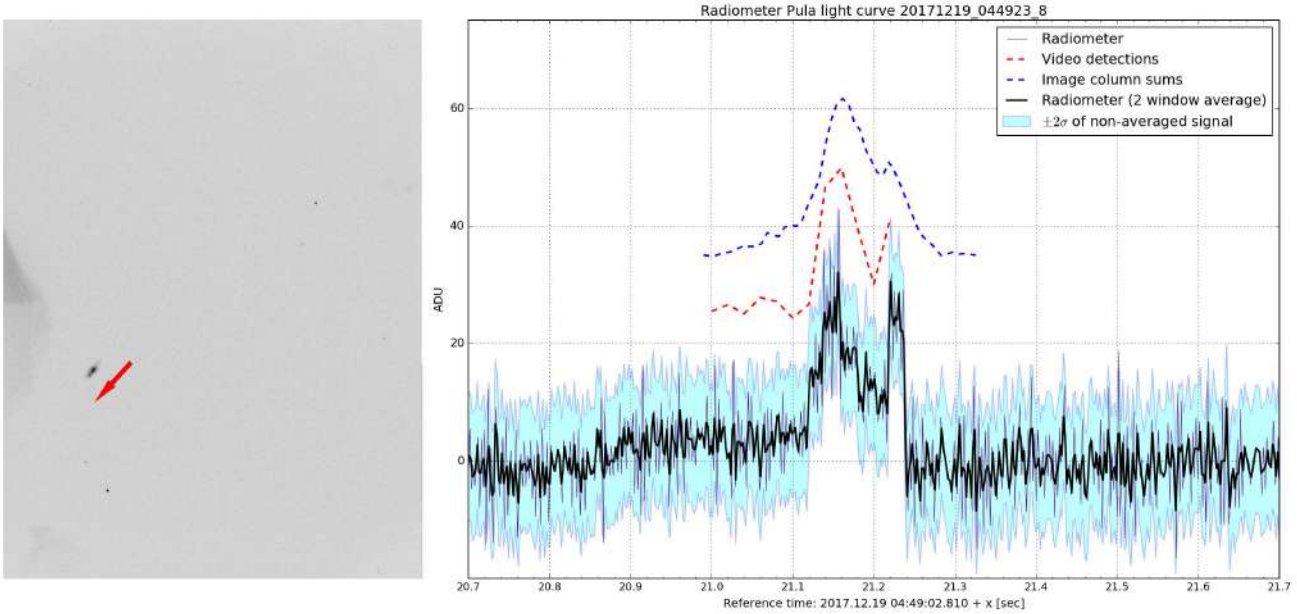

Figure 9 – 2017 December 19, $04^{h}49^{m}23^{s}$ fireball – video and radiometric lightcurve comparison.

Pujol J., Rydelek P., and Bohlen T. (2005). "Determination of the trajectory of a fireball using seismic network data". *Bulletin of the Seismological Society of America*, **95:4**, 1495–1509.

Šegon D., Vida D., Korlević K., and Andreić Ž. (2016). "Croatian Meteor Network: ongoing work 2015–2016". In *Proceedings of the International Meteor Conference 2016, Egmond, The Netherlands*. pages 270–274.

Shrbeny L. and Spurny P. (2013). "Determination of atmospheric velocity of bright meteors on the basis of high-resolution light curves". *Astronomy & Astrophysics*, **550**, A31.

Spurny P., Borovička J., and Shrbeny L. (2006). "Automation of the Czech part of the European fireball network: equipment, methods and first results". *Proceedings of the International Astronomical Union*, **2:S236**, 121–130.

Spurny P. and Ceplecha Z. (2008). "Is electric charge separation the main process for kinetic energy transformation into the meteor phenomenon?". *Astronomy & Astrophysics*, **489:1**, 449–454.

Spurny P., Spalding R. E., and Jacobs C. (2001). "Common ground-based optical and radiometric detections within Czech fireball network". In *Meteoroids 2001 Conference*, volume 495. pages 135–140.

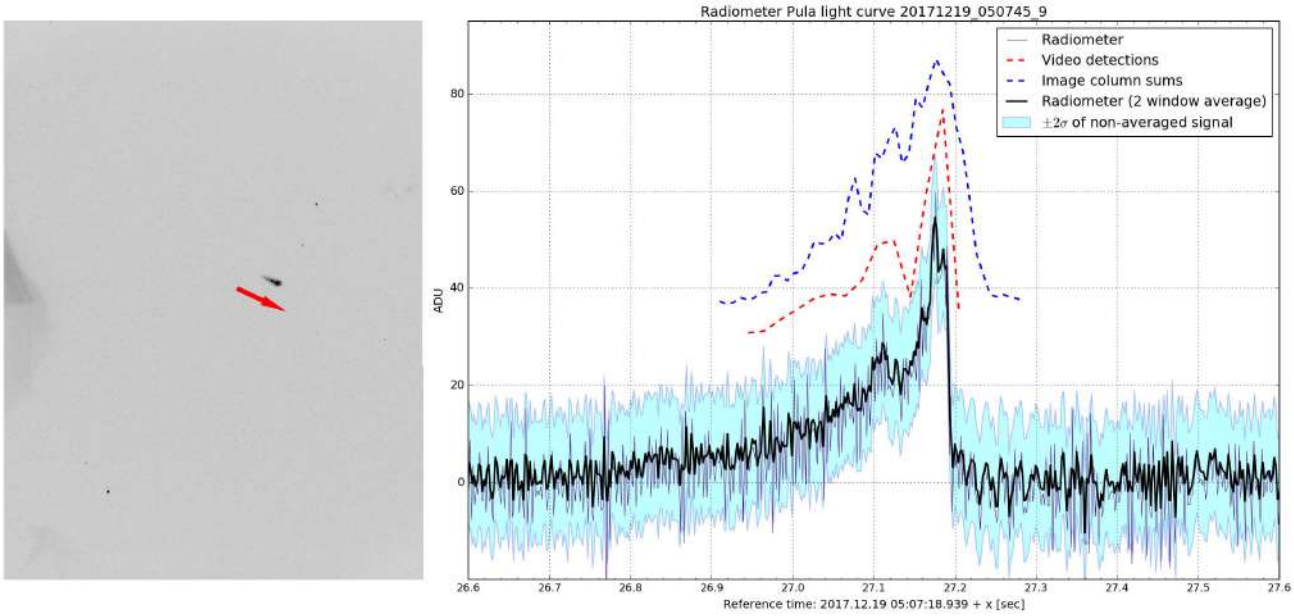

Figure 10 – 2017 December 19, $05^{h}07^{m}45^{s}$ fireball – video and radiometric lightcurve comparison.

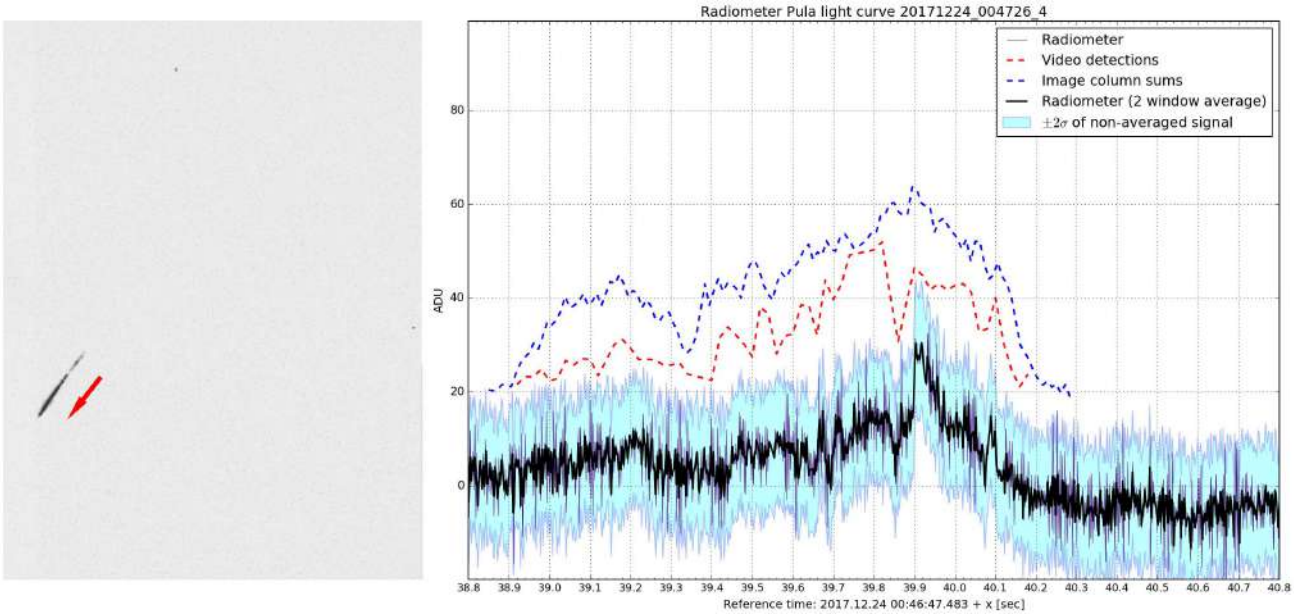

Figure 11 – 2017 December 24, $00^{h}47^{m}26^{s}$ fireball – video and radiometric lightcurve comparison.

Vida D., Turčinov R., Šegon D., and Silađi E. (2015). "Low-cost meteor radiometer". In *Proceedings of the International Meteor Conference, Mistelbach, Austria*. pages 27–30.

Williams A. B. and Taylor F. J. (1995). *Electronic filter design handbook*. McGraw-Hill.

Handling Editor: Javor Kac
This paper has been typeset from a LaTeX file prepared by the authors.

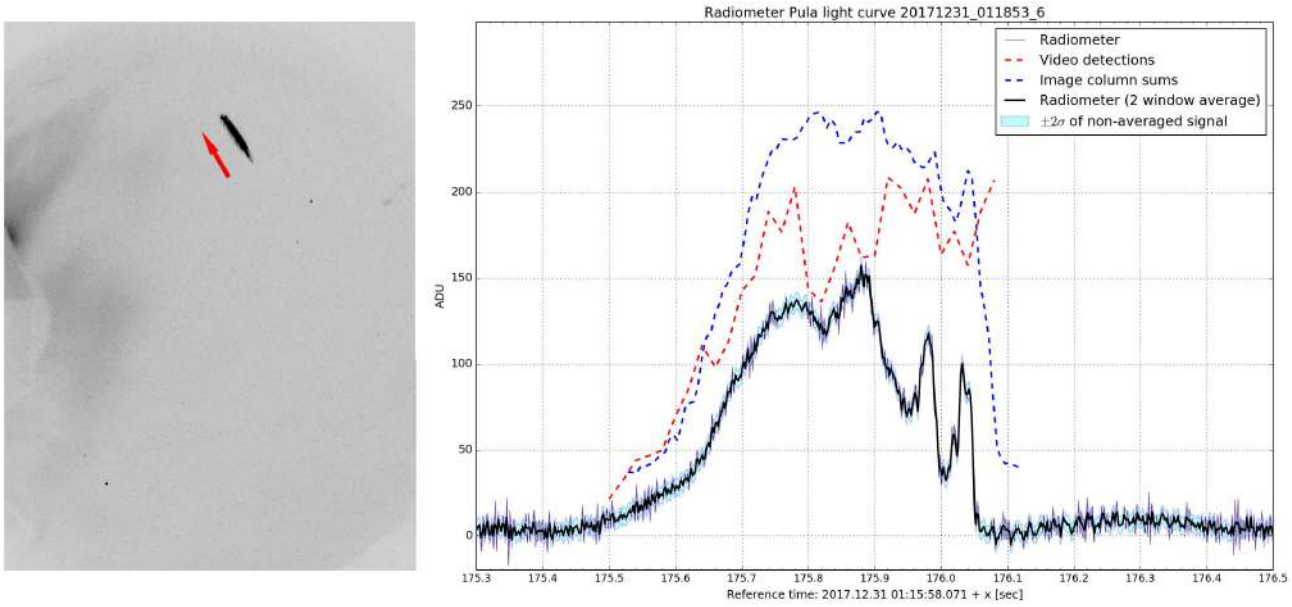

Figure 12 – 2017 December 31, $01^{h}18^{m}53^{s}$ fireball – video and radiometric lightcurve comparison.

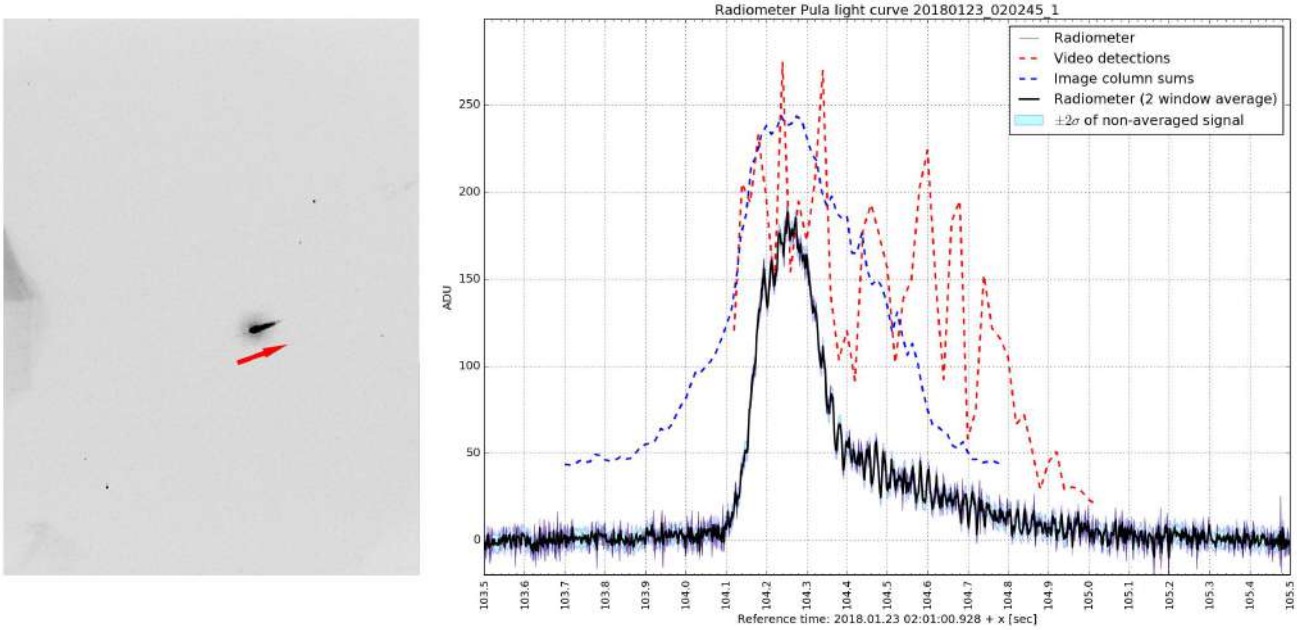

Figure 13 – 2018 January 23, $02^{h}02^{m}45^{s}$ fireball – video and radiometric lightcurve comparison.

Appendix

Parts list and schematics

A list of parts for the improved version of the radiometer is given in Table 2, while the schematics are given in Figures 14 and 15. The three 47 pF capacitors are soldered in parallel with 1 MΩ resistors (R2, R5, R9) at the bottom side of the board. Diodes D1, D2 and D3 are in fact jumpers leading to triples of diodes connected in parallel, but the schematic shows the correct orientation of the diodes. The gain of the amplifier is controlled using the potentiometer.

Table 2 – List of parts for the improved version of the low-cost radiometer.

Label	Part	Value/description	Quantity
C1	Electrolytic capacitor	47 µF, 25 V	1
C2, C3	Ceramic capacitor	0.1 μF, 25 V	2
—	Ceramic capacitor	47 pF, 25 V	3
R2, R5, R9	Resistor	1 MΩ, 1/8 W	3
R10, R11, R12, R15	Resistor	100 kΩ, 1/8 W	4
R1, R3, R4, R6, R7, R8, R14	Resistor	10 kΩ, 1/8 W	7
R13	Trimmer potentiometer	1 MΩ	1
D1 – D9	BPW34	DIP package	9
IC1	LMC6464	quad OP, DIP package	1
IC2	78L05	0.5 A	1
—	Pin headers	—	6
—	Jumper wires	—	6

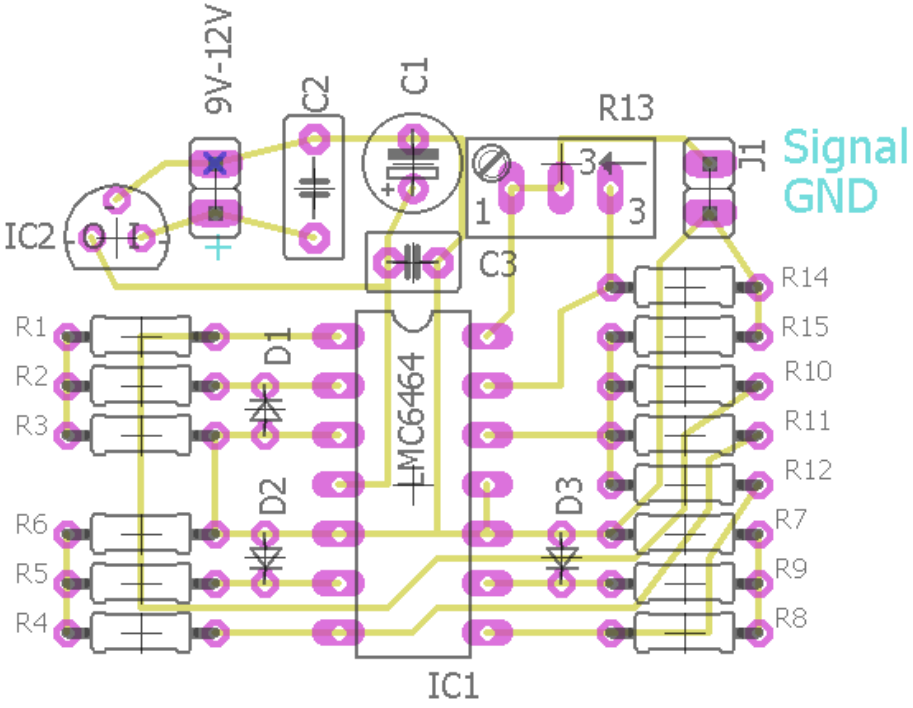

Figure 14 – Radiometer amplifier board schematics. "Signal" and "GND" are output pins which are connected to the DAQ board.

Figure 15 – Radiometer amplifier schematics. Pins 4 and 11 are +5V and GND power pins for LMC6464.

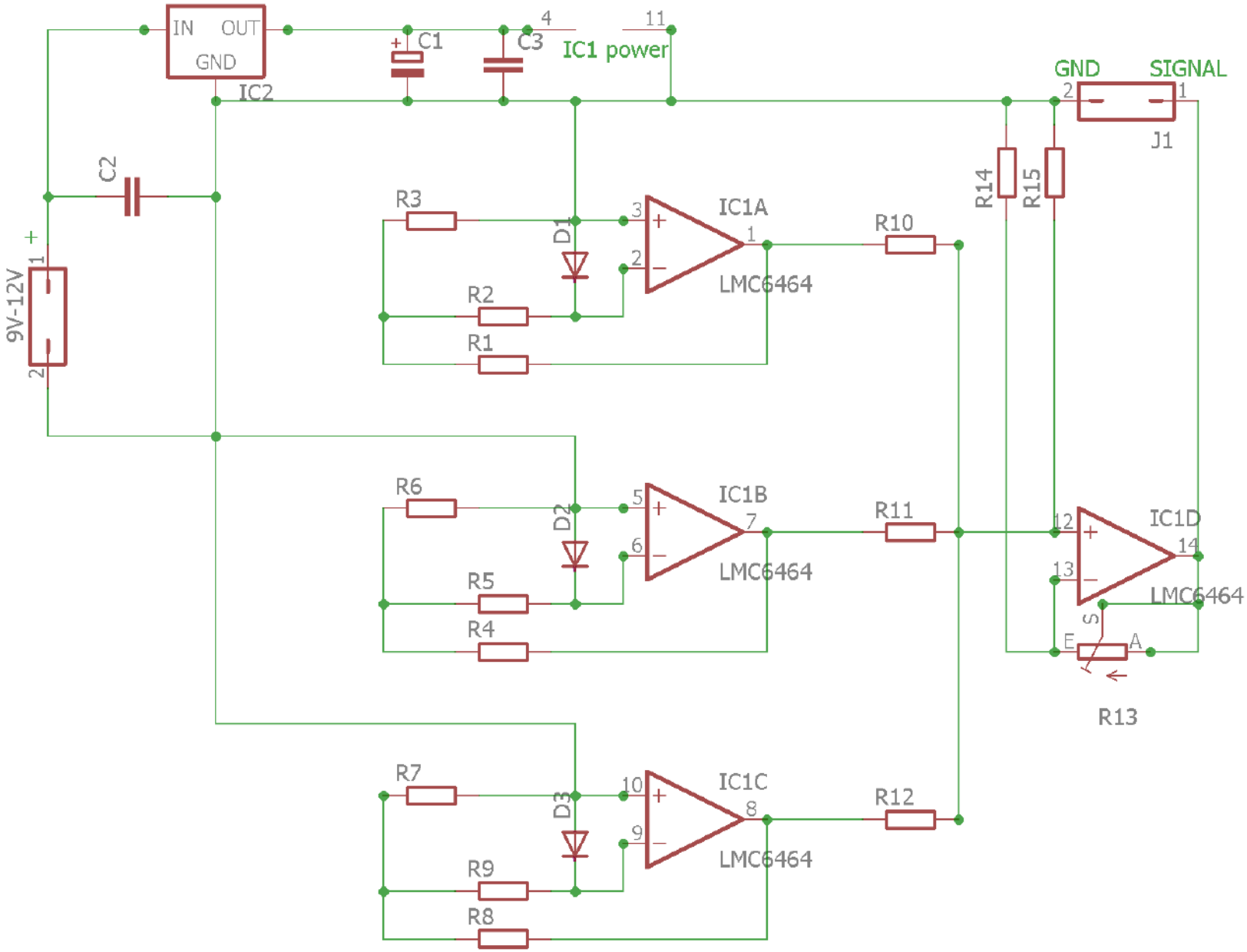

First results of a Raspberry Pi based meteor camera system

Denis Vida[1,2,3], *Michael J. Mazur*[1,2], *Damir Šegon*[4], *Dario Zubović*[5], *Patrik Kukić*[6], *Filip Parag*[7], *and Anton Macan*[5,8]

We present first orbital solution of a meteor estimated completely using open-source methods and software running on a Raspberry Pi single-board computer. Astrometry methods and tools are described in detail, and we find that our results compare well to independent Croatian Meteor Network observations and UFOOrbit trajectory estimation results. We explore a CMOS alternative to the recently discontinued Sony CCD low-light CCD sensors. Sensitivity, linearity of the sensor, and the quality of photometry are discussed.

Received 2018 February 1

1 Introduction

Following the development and wide availability of low-cost low-light security cameras, their potential for meteor observation was quickly realized by amateur astronomers (Gural & Segon, 2009; Samuels et al., 2014). Zubović et al. (2015) were the first to offer an alternative to using personal computers for automatic meteor data acquisition and processing by demonstrating that single-board computers such as the Raspberry Pi 2[a] are up to the task as well. Vida et al. (2016) presented open-source meteor detection software designed for single-board computers, which can run on personal computers as well, and laid out the roadmap towards a network of low-cost meteor stations. Early developments were documented as part of the Asteria Network project[b] which was organized for the 2015 Hackaday Prize. Subsequently, the development continued and the code remained available on GitHub[c]. In the end we have adopted the name RMS (Raspberry Pi Meteor Station) for the software, although the code runs fine on personal computers as well.

The main idea behind the project is to provide a reliable, low-cost replacement for existing meteor observation systems and offer improvements on proprietary and antiquated meteor detection software commonly used today. By making our code completely transparent and data acquired by the systems open, we hope to motivate the creation an international community of meteor astronomers, a global meteor network with large sky coverage and standardized methodology. We aim to develop modular systems based on moderate field-of-view cameras which can be deployed in a variety of configurations, from single camera to multi-camera all-sky arrangements, satisfying needs of most amateur astronomers. The software pipeline will be designed to provide near real-time reporting of meteor radiants and orbits which will be available to the general public, while the main goal is to have enough stations around the globe to acquire at least 1000 optical meteor orbits a night.

A large sky coverage is essential for answering fundamental questions in meteor science. Strong meteor shower outbursts are often of very short duration and are geographically localized, for example the 2011 February η Draconid outburst (Jenniskens & Gural, 2011), 2014 Camelopardalid outburst (Campbell-Brown et al., 2016), and the 2015 Taurid outburst (Spurny et al., 2017). Their short duration and localization make their observation precarious, creating a possibility of not optically observing an outburst at all due to unfavourable weather conditions. For example, the 2011 October Draconid outburst (Ye et al., 2013a) lasted only $\sim$ 4 hours, but was well observed visually both from the ground (Molau & Barentsen, 2014) and the air (Vaubaillon et al., 2015; Koten et al., 2014) due to previous predictions by Vaubaillon et al. (2011). On the other hand, the 2012 Draconid meteor storm ($\mathrm{ZHR}_{\max} \approx 9000 \pm 1000$ in radar sizes) was only noticed by chance by Ye et al. (2013b), while only real-time optical data was provided by visual observers on another continent, albeit with a much lower ZHR. The outburst was poorly observed optically – it was not observed by CAMS (Jenniskens et al., 2016), Toth et al. (2014) observed 28 Draconids but gave no details about the radiants, and Molau et al. (2013) reported a 90 minute peak of activity based on single-station observations. Ye et al. (2013b) show radiants with high dispersion, which is purely an observation bias due to low precision of radar measurements, while their dynamical simulations show very tight radiants. If high precision optical data was available, the simulations could have been better constrained and predictions of future outbursts made more reliable. Furthermore, a wide coverage may reduce observational biases for meteor shower flux statistics as well (Blaauw et al., 2016; Campbell-Brown & Braid, 2011). Finally, meteor showers with very low flux can possibly be discovered simply due to the larger number statistics.

[1]Department of Earth Sciences, University of Western Ontario, London, Ontario, N6A 5B7, Canada.
[2]Department of Physics and Astronomy, University of Western Ontario, London, Ontario, N6A 3K7, Canada.
[3]Email: dvida@uwo.ca
[4]Astronomical Society Istra Pula, Park Monte Zaro 2, HR-52100 Pula, Croatia
[5]Croatian Meteor Network
[6]XV Gymnasium, Jordanovac 8, HR-10000 Zagreb, Croatia
[7]Petnica Science Center, RS-14104 Valjevo, Serbia
[8]Grammar school "Gimnazija Pula", Trierska 8, HR-52100 Pula, Croatia

IMO bibcode WGN-462-vida-rms
NASA-ADS bibcode 2018JIMO...46...71V

[a]Raspberry Pi 2 – https://www.raspberrypi.org/products/raspberry-pi-2-model-b/ (Accessed December 28, 2017)
[b]Hackaday.io – Asteria network https://hackaday.io/project/6811-asteria-network, (Accessed December 28, 2017)
[c]RMS source code on GitHub, https://github.com/CroatianMeteorNetwork/RMS, (Accessed December 28, 2017)

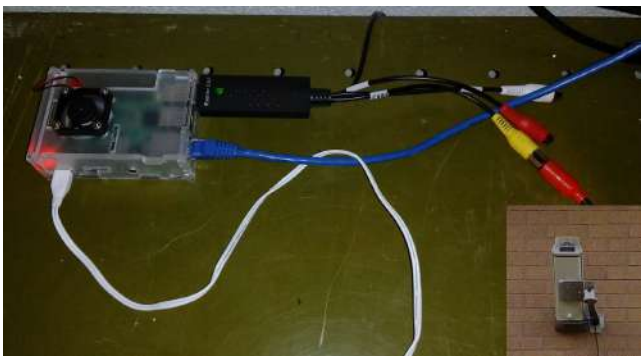

Figure 1 – Raspberry Pi system at Elginfield.

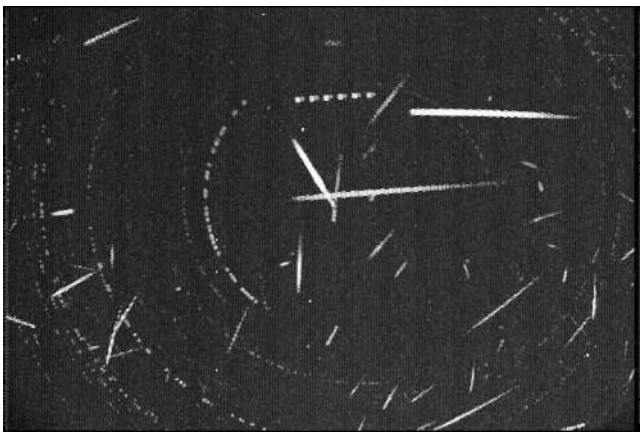

Figure 2 – 54 meteors detected on the night of July 29^{th} to 30^{th}, 2017 with the Elginfield system.

A dense global meteor network would result in an increase of instrumentally observed meteorite falls – currently only about 30 meteorites have known orbits (Spurny, 2015). Also, more data would be collected on very rare simultaneous meteors which fragment before entering the atmosphere (Koten et al., 2017).

Finally, atmospheric phenomena like sprites and blue jets can be observed with such systems, enabling their localization and connection to discharges in the lower atmosphere (Wescott et al., 2001), as well as meteor-triggered high-atmosphere discharges (Suszcynsky et al., 1999).

In this work we present the current progress of both hardware and software development, first concrete results and orbits, and plans for expansion of the network in the near future.

2 Current software and hardware status

At the time of publication of this article, systems running our code were operational in Canada, Croatia, France and the Netherlands, while testing is being conducted in Brazil, Germany and Korea. The first permanent meteor station running our software was deployed in June 2017 at Elginfield Observatory, north of London, Ontario (Canada). The system consists of an analog Sony Effio 673 CCD camera, EasyCap video digitizer, and a Raspberry Pi 3 single-board computer (Figure 1). This system was used as a test bed for new features and stability tests. Detailed instructions on how to build such a system were published on the Instructables website[d]. At the time of writing of this article, the system has reliably captured meteors for months without interruption or errors, requiring no external intervention. Figure 2 shows the stack of images of 54 meteors detected in one night in late July 2017.

3 Updated processing pipeline

The data processing pipeline has been updated since the work presented in Vida et al. (2016) to include automatic astrometric calibration, data management and uploading calibrated meteor detections to a central server located at the University of Western Ontario. Figure 3 shows a diagram of the updated pipeline. With properly configured software, it will wait until sundown (when the Sun is 5.5° below the horizon) to start capturing. Two memory buffers, each the size of 256 video frames, are initialized and the video stream is alternated between them. When the first block of 256 is full, Four-frame Temporal Pixel (FTP) compression (Gural, 2011) is performed on them, after which real-time fireball detection is performed as well. Due to compression artifacts produced by the FTP compression on very bright events it is preferable to extract and store raw video frames of such bright events for later analysis. This procedure is described in more detail in (Vida et al., 2016).

All FTP compressed files are put on a queue from which they are relayed to threads running star extraction and meteor detection. As these tasks are more computationally intensive, they are not performed in real time and are left to run after sunrise. Only one detection thread is running during video capture, while two more are spawned after it ends at sunrise.

The detection often finishes within one hour after sunrise, after which automatic recalibration of astrometric parameters is performed. In summary, 5 parameters define the basic astrometric solution (centre of the field of view): reference Julian date JD_{ref}, equatorial coordinates of the field-of-view (FOV) centre α_{ref} and δ_{ref} at JD_{ref}, pixel scale, and reference position angle. The distortion is estimated using 3^{rd} order polynomials with an added radial distortion term (12 additional parameters, for details see Vida et al. (2016)). The parameter refinement is stopped upon finding a set of astrometric parameters which produce the smallest average residual between the predicted and the observed positions of stars, or it is stopped when the average residual becomes smaller than 1/3 of a pixel – this precision is achieved most nights. We also consider the number of matched stars as an indicator of the quality of the fit, thus we have defined the cost function for minimization as:

$$C = \frac{\bar{d}^2}{\sqrt{N_{matched} + 1}} \quad (1)$$

[d]Building a Raspberry Pi meteor station: http://www.instructables.com/id/Raspberry-Pi-Meteor-Station/ (Accessed December 30, 2017)

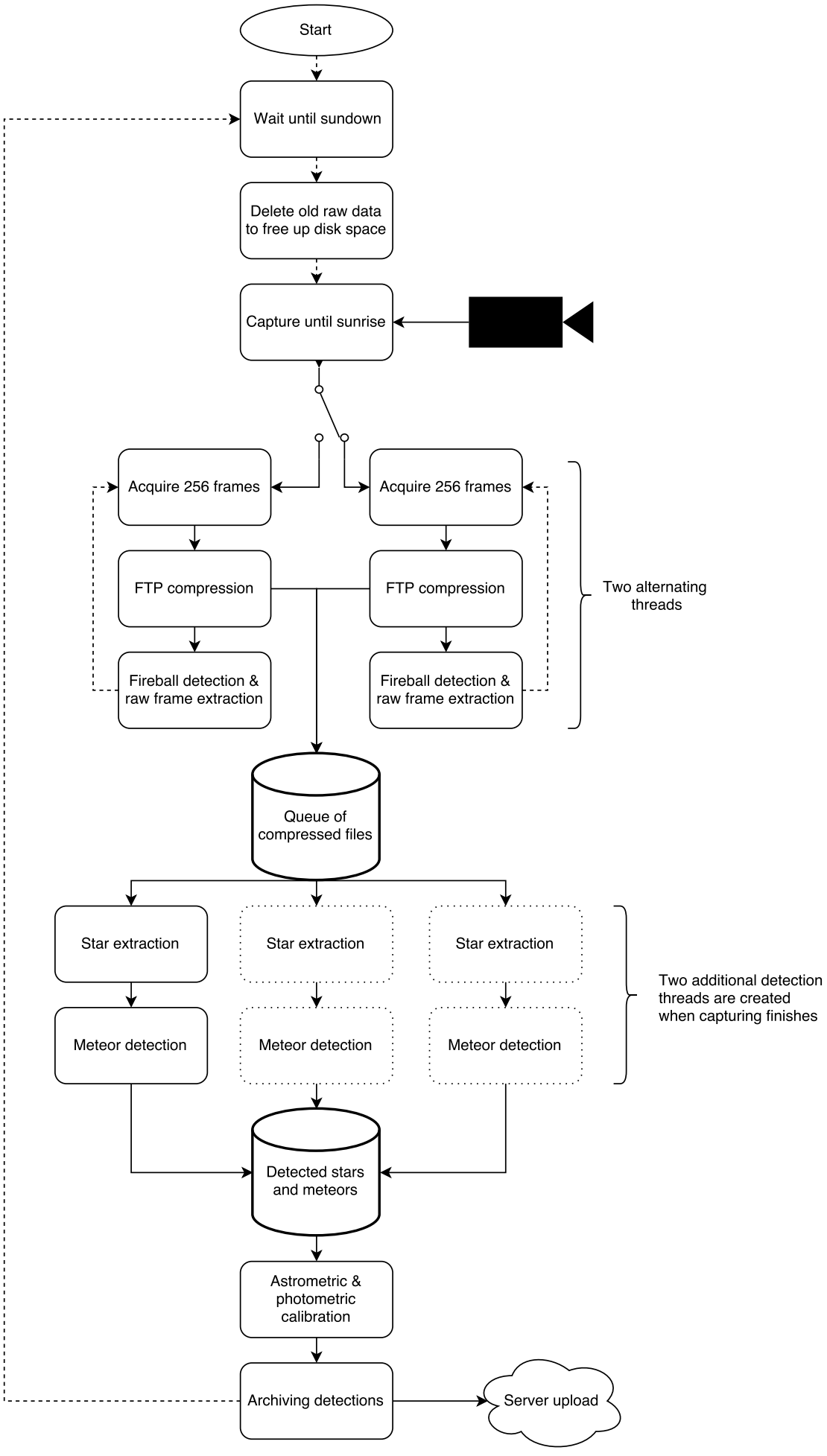

Figure 3 – Updated data processing pipeline.

where $\bar{d}$ is the average residual between predicted and observed positions of stars (in pixels), while $N_{matched}$ is the number of matched stars. The matching between catalog and image stars is done iteratively, starting with a star matching radius of 10 pixels. Next, it is reduced to 3, 1.5, and finally to 0.5 pixels. Image stars which are within this radius will be matched to catalog stars – the largest radius is most useful when the camera has been slightly shifted, so the automatic recalibration will succeed in those cases as well. After minimization with a certain matching radius is performed, this radius is decreased and a smaller number of false matches should be present in every subsequent iteration. Similarly to Šegon (2009), we use a subset of several thousands of stars detected throughout the night for astrometric calibration, which makes the fit more robust.

Finally, image centroids of detected meteors are converted to celestial coordinates with the refined astrometric solution, the photometry is performed, and the detections are archived and uploaded to the central server.

4 Creating an initial astrometric plate

The astrometry calibration process described above requires an initial astrometric plate which can be created with SkyFit, a program that is a part of our software package. The procedure begins by loading FTP compressed images into SkyFit and the user is prompted to enter an approximate altitude and azimuth of the centre of the FOV of the camera. The catalog stars are then projected on the image and the user can manually adjust the basic astrometric parameters (right ascension and declination of the FOV centre, scale, and image rotation). When the catalog stars are near the image stars, the user can manually pick and match image stars to catalog stars. At least 14 stars are needed for a robust fit. Figure 4 shows a screen shot of SkyFit during manual star picking and matching. Once enough stars are picked, the plate fit procedure is performed. Photometry fit can be viewed in a separate window.

In the future, we plan to host a public service on our server for automatic estimation of astrometric parameters which will be based on `astrometry.net` (Lang et al., 2010). This service will make SkyFit obsolete, but until then, it will be the preferred way of creating astrometric plates.

5 Orbit estimation results

In August 2017, during the Višnjan School of Astronomy (VSA) in Croatia, first multi-station tests with two temporary stations were conducted. One station was located in Višnjan and one in Pula, with 45 km between them. The Višnjan station consisted of four Sony Effio 673 cameras, two with 4 mm and two with 16 mm lenses, while the station in Pula consisted of one camera with a 6 mm lens. During several days of data collection, only a few common meteors between these stations were recorded, mainly due to poor volume overlap and unreliability of the code at the time. The first common meteor was captured on August 19

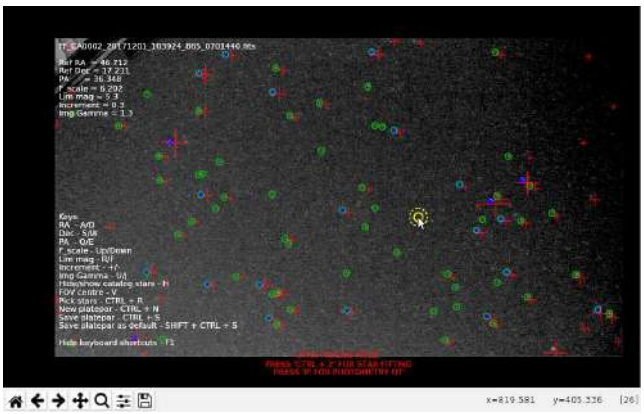

Figure 4 – SkyFit during star matching. Red crosses are catalog stars and their size reflects the magnitude, blue Xs are matched image stars and green circles are stars that were automatically detected on the image with our star extraction algorithm. The yellow circle is mouse cursor position (concentric circles are the annulus for centroiding whose size can be changed).

at $00^h10^m46^s$ UT above the Adriatic sea. Using the methods of Ceplecha (1987) and Borovicka (1990) we have estimated the trajectory and the orbit of the meteor, while the uncertainties of every parameter were estimated by adding Gaussian noise equivalent to the measurement error (see Figure 5, the measurement error was about 0.5 arc minute) to the data and running 50 Monte Carlo iterations. The same meteor was independently captured by four stations of the Croatian Meteor Network (CMN) and its orbit was estimated using UFOOrbit[e] software. Table 1 shows the comparison of the two orbit solutions. The orbits are very similar, most parameters were within one standard deviation from each other. We consider this independent confirmation as a proof of quality of data produced by our software, especially when considering that the convergence angle (Q_C in Table 1) of our solution was only about 15°, while the CMN solution had a significantly better geometry. The orbital solution indicates that the meteor was a sporadic from the apex source.

[e]UFOOrbit software, `http://sonotaco.com/soft/e_index.html`, Accessed December 31, 2017

Table 1 – Comparison of orbital elements of a meteor recorded on 2017 August 19 at $00^h10^m46^s$ UT. In the CMN column are the orbital parameters obtained using Croatian Meteor Network data and UFOOrbit, while the RMS column lists orbital parameters estimated with our software.

	CMN	RMS
Q_c	74.52°	15.99°
RA_G	48.679°	$48.436 \pm 0.244°$
Dec_G	+8.757°	$+8.656 \pm 0.029°$
V_G	66.920 km s^{-1}	66.780 ± 0.305 km s^{-1}
a	3.379 AU	3.265 ± 0.218 AU
e	0.719	0.712 ± 0.027
i	163.930°	$163.806 \pm 0.157°$
ω	31.533°	$33.683 \pm 0.156°$
Ω	325.983°	$326.300 \pm 0.0002°$

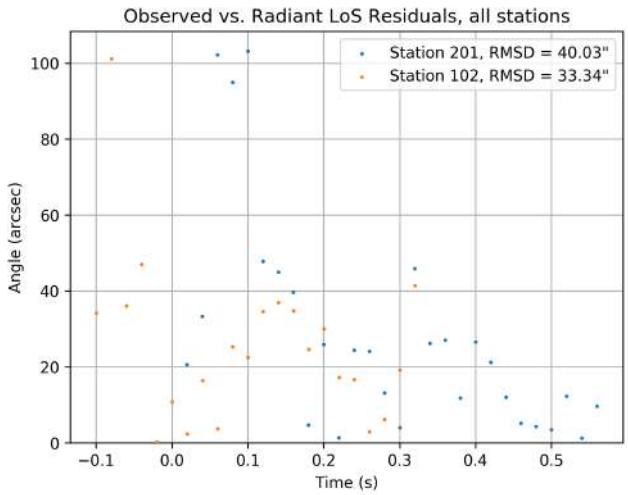

Figure 5 – Trajectory angular residuals of the 2017 August 19, $00^h10^m46^s$ UT meteor, observations with Raspberry Pi systems. The standard deviation of observations from the fit was about half an arc minute. Pixel scale for station 102 (Višnjan) was 5.3 ' px^{-1}, while for station 201 (Pula) it was 3.5 ' px^{-1}.

6 Feasibility of CMOS IP cameras for meteor work

In 2015 Sony announced[f] that they will discontinue manufacturing all CCD sensors in March 2017 and completely focus on CMOS sensors. This news will have a significant impact on meteor video observations, as practically all major networks are using cameras with Sony CCD chips (Jenniskens et al., 2011; Brown et al., 2010; Tóth et al., 2015). Furthermore, it is to be expected that the lower price range, explored by Samuels et al. (2014), will be most affected as it will take time for the new technology to come down in price. So far, a viable low-cost alternative has not been explored for meteor purposes and several concerns remain – mainly about the sensitivity and linearity of CMOS sensors, which may affect the quality of meteor photometry. Furthermore, many CMOS sensors at the lower price range (below $100 USD) have a rolling shutter, while global shutter cameras are only found in the upper price range. In rolling shutter cameras each row of pixels starts its integration in a staggered fashion from top to bottom over the frame time, thus each row represents a different time start/slice relative to its neighbors. On the other hand, in global shutter cameras all pixels start and stop their integration simultaneously. Here we explore one low-cost CMOS sensor, the Sony IMX225, and discuss its feasibility for video meteor work.

We have tested a digital IP camera with the IMX225[g] sensor and the HI3518E DSP. The camera has a resolution of 1280×720, compresses the video stream with the H.264 compression and is capable of frame rates up to 25 frames per second. An analog HD version of the camera is available as well. We have found that Raspberry Pi 3 supports hardware decoding of H.264 video, which adds near-zero overhead to the processing time, despite the total number of pixels being more than two times larger compared to lower resolution video from EasyCap devices (720×576). The sensor is 12-bit, but the images are downsampled to 8 bits during the H.264 compression.

Figure 6 – A meteor captured with the IMX225 CMOS camera. Visible constellations are Gemini (centre) and Auriga (right). The image is a 10.24 s maxpixel obtained using the Four-frame temporal pixel compression method.

Hankey and Perlerin (2018) tested the IMX290[h] camera, while IMX174[i] is being tested by Pete Gural (private communication). By looking at their stated specifications, the IMX225 is the most sensitive of all, having a sensitivity of 2350 mV at 1/30 s exposure, compared to 1300 mV for IMX290 and 825 mV for IMX174, although the IMX174 has a larger sensor and pixel pitch size. Furthermore, other advantages of the IMX225 is that the sensor is progressive scan (no interleave) and the IP board versions of the camera can be bought for as little as $20 USD, which make it a good candidate for testing. We have equipped the camera with a 4 mm lens ($64° \times 36°$ FOV, ~ 3 ' px^{-1} scale) and found that the camera is more than sensitive enough for video meteor purposes, with the gain set to 50% more than half the detected meteors were saturating, while the stellar limiting magnitude was about $+5.5^M$ from London, Ontario (Canada), which is under heavily light polluted skies. In the end, we have settled on 20% gain which gave a stellar limiting magnitude of about $+5.3^M$, with no major loss in the number of detected meteors, but with improved dynamic range. Figure 6 shows an example of one captured meteor with the setup.

Next, we explored the quality of photometry as there are concerns about linearity of CMOS sensors. We used stars from the SKY2000v5 catalog (Myers et al., 2015) for photometric calibration, which lists Johnson-Cousins magnitudes in U, B, V, R and I bands (Johnson & Morgan, 1953; Cousins, 1976). Not all stars have entries for R and I bands, thus we have derived them from

[f]IMPERIX response to Sony's CCD manufacture discontinuation, `https://www.imperx.com/latest-news/sony-discontinues-ccd-image-sensors/`, (Accessed December 31, 2017)

[g]IMX225 Sony website, `http://www.sony-semicon.co.jp/products_en/new_pro/october_2014/imx224_225_e.html` (Accessed January 1, 2018)

[h]IMX290 Sony website, `http://www.sony-semicon.co.jp/products_en/new_pro/february_2015/imx290_291_e.html` (Accessed January 1, 2018)

[i]IMX174 Sony website, `http://www.sony-semicon.co.jp/products_en/new_pro/december_2013/imx174_e.html` (Accessed January 1, 2018)

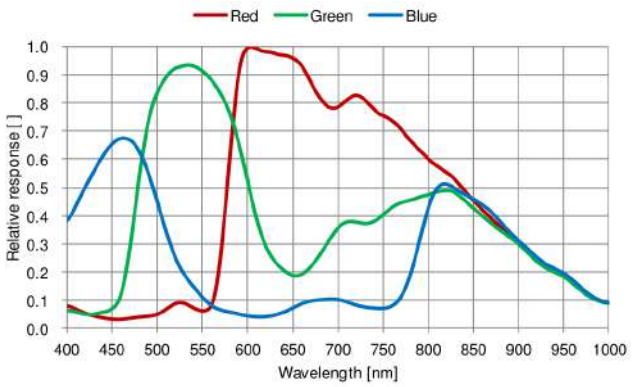

Figure 7 – IMX225 spectral response. The sensor uses a standard Bayer filter and during the conversion from color to B/W, the green channel is added in twice: $I_{BW} = R + 2G + B$. Source: IMX225 datasheet.

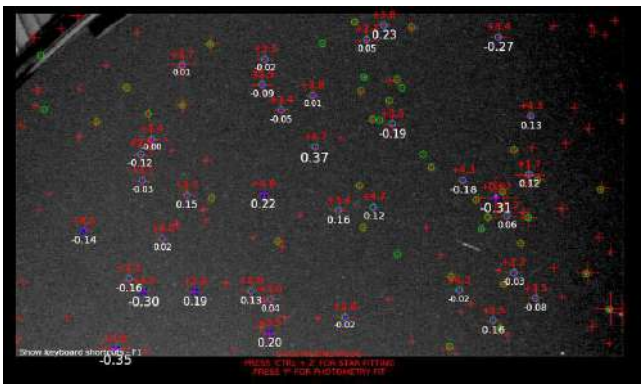

Figure 8 – Photometry done in SkyFit. Red numbers above stars are catalog magnitudes in our instrumental band, while white numbers below the stars are deviations in magnitude from the fit.

V and B magnitudes, following the method of Caldwell et al. (1993). After performing a fit on stars which had entries for magnitudes in all bands we arrived at the following relation for R magnitudes:

$$R = V - 0.77(B - V) - 0.04 \quad (2)$$

We have estimated I magnitudes by following Natali et al. (1994):

$$I = B - 2.36(B - V) \quad (3)$$

Following the method of Jenniskens et al. (2011), we have estimated the instrumental magnitude from the spectral response of the IMX225 sensor (Figure 7) as $0.10B + 0.32V + 0.23R + 0.35I$. Photometry was done without vignetting correction and with no flat field applied to the image. Figure 8 shows the stars chosen for photometry, while Figure 9 shows the photometric fit. The scatter at fainter magnitudes is due to the lower signal-to-noise ratio at those magnitudes, while at brighter magnitudes saturation effects appear. Nevertheless, the fit is linear between magnitude 0 and 5, while saturation correction will be needed for brighter meteors. We find that in the linear response region the quality of fit (1σ of $\pm 0.17^M$) is similar to the CAMS photometric fit given in Jenniskens et al. (2011), which used analog CCD cameras for data collection. The H.264 compression does not seem to have adverse effects on the photometry of stars, while comparison of meteor photometry from several stations will be done in the future.

Finally, the only concern that remains is the influence of the rolling shutter on the centroids of meteors as they move across the image plane. Early results of simulations are showing that it is negligible for slow meteors and meteors moving near-horizontally across the image plane, which means that the effect should be minimal for all-sky FOVs but may be of concern for moderate to narrow FOVs. This will be thoroughly explored in a future paper and a correction for the effect will be given.

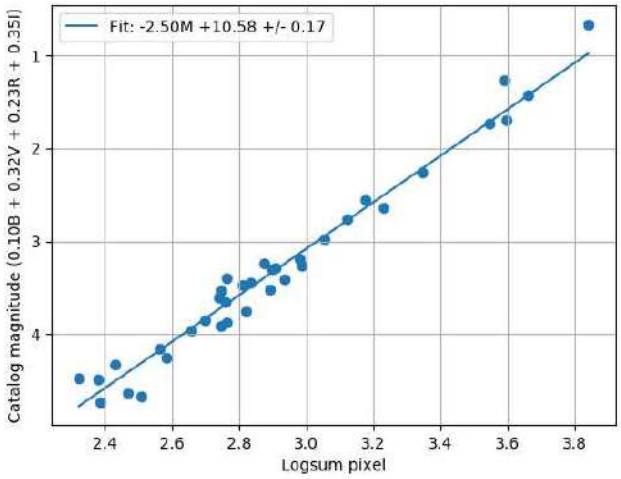

Figure 9 – Photometry fit on stars shown in Figure 8.

7 Conclusion

We have presented an updated pipeline of the RMS software, demonstrated sufficient quality of astrometry and verified the implementation by comparing an orbit obtained using our software with Croatian Meteor Network observations of the same meteor. The orbit matches well and is within one standard deviation of the orbit independently estimated with UFOOrbit.

We have found a possible CMOS replacement for low-light CCD sensors that are in use before but are no longer manufactured. The IMX225 camera was shown to be sensitive enough for meteor work (stellar limiting magnitude of $+5.3^M$ with a 4 mm $f/1.2$ lens from a heavily light polluted location), and the camera response is linear for a range of 5 magnitudes. The only remaining concern is the influence of the rolling shutter on meteor centroids, but the correction method is being developed and will be published soon. The short-term plan is to set up a permanent multi-station configuration for trajectory estimation testing, and to grow the network globally in the long term. Interested individuals are encouraged to contact the authors for more information as meteor station kits running our software will be available on the market in the near future.

8 Acknowledgements

We thank Dr. Peter Brown for financially supporting the project. Also many thanks to Peter Gural for many invaluable advice and reviewing the manuscript of this paper, and Aleksandar Merlak for hosting and testing CMOS cameras. We are grateful to Dr. Cees Bassa for finding bugs in the code and writing extensions for satellite tracking. Finally, we would to thank Dr. Tobias Cornelius Hinse and Jean-Marie Jacquart for suggestions and independent testing of our software.

9 Author Contributions

DV wrote the paper and most of the RMS code. MJM worked on hardware development, installation and testing. DŠ procured the hardware used at VSA2017 and provided many useful suggestions. DZ helped solve obstacles in the code which seemed insurmountable at the time. PK, FP and AM participated in VSA2017 where they helped to build hardware, install systems, collect and analyze data.

References

Blaauw R., Campbell-Brown M., and Kingery A. (2016). "Optical meteor fluxes and application to the 2015 Perseids". *Monthly Notices of the Royal Astronomical Society*, **463:1**, 441–448.

Borovicka J. (1990). "The comparison of two methods of determining meteor trajectories from photographs". *Bulletin of the Astronomical Institutes of Czechoslovakia*, **41**, 391–396.

Brown P., Weryk R., Kohut S., Edwards W., and Krzeminski Z. (2010). "Development of an all-sky video meteor network in Southern Ontario, Canada The ASGARD System". *WGN, Journal of the International Meteor Organization*, **38**, 25–30.

Caldwell J., Cousins A., Ahlers C., Van Wamelen P., and Maritz E. (1993). "Statistical relations between the photometric colours of common types of stars in the UBV (RI) c, JHK, and uvby systems". *South African Astronomical Observatory Circular*, **15**, 1.

Campbell-Brown M., Blaauw R., and Kingery A. (2016). "Optical fluxes and meteor properties of the camelopardalid meteor shower". *Icarus*, **277**, 141–153.

Campbell-Brown M. and Braid D. (2011). "Video meteor fluxes". *Meteoroids: The Smallest Solar System Bodies*, **NASA/CP-2011-216469**, 304–312.

Ceplecha Z. (1987). "Geometric, dynamic, orbital and photometric data on meteoroids from photographic fireball networks". *Bulletin of the Astronomical Institutes of Czechoslovakia*, **38**, 222–234.

Cousins A. (1976). "VRI standards in the E regions". *Memoirs of the Royal Astronomical Society*, **81**, 25.

Gural P. (2011). "The California all-sky meteor surveillance (CAMS) system". In *Proceedings of the International Meteor Conference, 29th IMC, Armagh, Northern Ireland, 2010*. pages 28–31.

Gural P. and Segon D. (2009). "A new meteor detection processing approach for observations collected by the Croatian Meteor Network (CMN)". *WGN, Journal of the International Meteor Organization*, **37**, 28–32.

Hankey M. and Perlerin V. (2018). "AMS Fireball Program". In *Proceedings of the International Meteor Conference, Petnica, Serbia, 2017*. page TBD.

Jenniskens P., Gural P., Dynneson L., Grigsby B., Newman K., Borden M., Koop M., and Holman D. (2011). "CAMS: Cameras for Allsky Meteor Surveillance to establish minor meteor showers". *Icarus*, **216:1**, 40–61.

Jenniskens P. and Gural P. S. (2011). "Discovery of the February Eta Draconids (FED, IAU# 427): the dust trail of a potentially hazardous long-period comet". *WGN, Journal of the IMO*, **39**, 93–97.

Jenniskens P., Nénon Q., Albers J., Gural P., Haberman B., Holman D., Morales R., Grigsby B., Samuels D., and Johannink C. (2016). "The established meteor showers as observed by CAMS". *Icarus*, **266**, 331–354.

Johnson H. and Morgan W. (1953). "Fundamental stellar photometry for standards of spectral type on the revised system of the Yerkes spectral atlas". *The Astrophysical Journal*, **117**, 313.

Koten P., Čapek D., Spurny P., Vaubaillon J., Popek M., and Shrbenỳ L. (2017). "September epsilon Perseid cluster as a result of orbital fragmentation". *Astronomy & Astrophysics*, **600**, A74.

Koten P., Vaubaillon J., Tóth J., Margonis A., and Ďuriš F. (2014). "Three peaks of 2011 Draconid activity including that connected with pre-1900 material". *Earth, Moon, and Planets*, **112:1-4**, 15–31.

Lang D., Hogg D. W., Mierle K., Blanton M., and Roweis S. (2010). "Astrometry. net: Blind astrometric calibration of arbitrary astronomical images". *The astronomical journal*, **139:5**, 1782.

Molau S. and Barentsen G. (2014). "Real-time flux density measurements of the 2011 Draconid meteor outburst". *Earth, Moon, and Planets*, **112:1-4**, 1–5.

Molau S., Kac J., Berko E., Crivello S., Stomeo E., Igaz A., Barentsen G., and Goncalves R. (2013). "Results of the IMO Video Meteor Network – October 2012". *WGN, Journal of the International Meteor Organization*, **41**, 23–30.

Myers J., Sande C., Miller A., Warren Jr W., and Tracewell D. (2015). "VizieR Online Data Catalog: SKY2000 Master Catalog, Version 5 (Myers+ 2006)". *VizieR Online Data Catalog*, **5145**.

Natali F., Natali G., Pompei E., and Pedichini F. (1994). "The use of the (BI) color index and applications of the (BI) versus (BV) relationship". *Astronomy and Astrophysics*, **289**, 756–762.

Samuels D., Wray J., Gural P. S., and Jenniskens P. (2014). "Performance of new low-cost 1/3" security cameras for meteor surveillance". In *Proceedings of the 2014 International Meteor Conference, Giron, France*. pages 18–21.

Spurny P. (2015). "Instrumentally documented meteorite falls: two recent cases and statistics from all falls". *Proceedings of the International Astronomical Union*, **10:S318**, 69–79.

Spurny P., Borovička J., Mucke H., and Svoreň J. (2017). "Discovery of a new branch of the Taurid meteoroid stream as a real source of potentially hazardous bodies". *Astronomy & Astrophysics*, **605**, A68.

Suszcynsky D., Strabley R., Roussel-Dupre R., Symbalisty E., Armstrong R., Lyons W., and Taylor M. (1999). "Video and photometric observations of a sprite in coincidence with a meteor-triggered jet event". *Journal of Geophysical Research: Atmospheres*, **104:D24**, 31361–31367.

Tóth J., Kornoš L., Zigo P., Gajdoš Š., Kalmančok D., Világi J., Šimon J., Vereš P., Šilha J., Buček M., et al. (2015). "All-sky Meteor Orbit System AMOS and preliminary analysis of three unusual meteor showers". *Planetary and space science*, **118**, 102–106.

Tóth J., Koukal J., Piffl R., Gajdoš Š., Zoladek P., Wisniewski M., Igaz A., Zigo P., Kornoš L., Kalmancok D., et al. (2014). "Draconids 2012—Unexpected outburst". In *Proceedings of the International Meteor Conference, Poznan, Poland, 22-25 August 2013*. pages 179–180.

Vaubaillon J., Koten P., Margonis A., Toth J., Rudawska R., Gritsevich M., Zender J., McAuliffe J., Pautet P.-D., Jenniskens P., et al. (2015). "The 2011 Draconids: the first European airborne meteor observation campaign". *Earth, Moon, and Planets*, **114:3-4**, 137–157.

Vaubaillon J., Watanabe J., Sato M., Horii S., and Koten P. (2011). "The coming 2011 Draconids meteor shower". *WGN, Journal of the IMO*, **39**, 3–59.

Vida D., Zubović D., Šegon D., Gural P., and Cupec R. (2016). "Open-source meteor detection software for low-cost single-board computers". *Proceedings of the IMC2016, Egmond, The Netherlands, u postupku objave*, pages 307–318.

Šegon D. (2009). "How many stars are needed for a good camera calibration?". *WGN, Journal of the International Meteor Organization*, **37**, 80–83.

Wescott E., Stenbaek-Nielsen H., Sentman D., Heavner M., Moudry D., and Sao Sabbas F. (2001). "Triangulation of sprites, associated halos and their possible relation to causative lightning and micrometeors". *Journal of Geophysical Research: Space Physics*, **106:A6**, 10467–10477.

Ye Q., Brown P. G., Campbell-Brown M. D., and Weryk R. J. (2013a). "Radar observations of the 2011 October Draconid outburst". *Monthly Notices of the Royal Astronomical Society*, **436:1**, 675–689.

Ye Q., Wiegert P. A., Brown P. G., Campbell-Brown M. D., and Weryk R. J. (2013b). "The unexpected 2012 Draconid meteor storm". *Monthly Notices of the Royal Astronomical Society*, **437:4**, 3812–3823.

Zubović D., Vida D., Gural P., and Šegon D. (2015). "Advances in the development of a low-cost video meteor station". In *Proceedings of the International Meteor Conference, Mistelbach, Austria*. pages 27–30.

Handling Editor: Javor Kac

This paper has been typeset from a LaTeX file prepared by the authors.

A new meteor shower, the Alpha Aquariids (#927:AAQ)

Yasuo Shiba, Chikara Shimoda, Kouji Maeda, SonotaCo, Takashi Sekiguchi, Kazuhiko Yoneguchi, Hiroshi Kawakami, Terunori Miyoshi, H. Yamakawa, Sadao Okamoto, Hideaki Muroishi, T. Masuzawa, and Toshio Kamimura [1]

We report a new meteor shower detection by the Japanese automatic TV meteor observation network "SonotaCo network". Four meteors appeared in 2017 October at solar longitude from 213 to 214 degrees (J2000.0) whose mean radiant position was right ascension 328.1 degrees and declination +0.4 degrees. These four meteors had common features (melting meteor) which were that the luminous trail lengthened at the middle way of the luminous path, and furthermore that beginning heights were higher. The brightest meteor (−2.4 absolute magnitude) produced a persistent train despite the especially slow initial velocity 13.1 km/s. This meteor shower had not been detected clearly from 2007 to 2016 in SonotaCo network observations.

Received 2018 March 10

1 Observation

This research is based on an automatic TV meteor observation network in Japan, the "SonotaCo network" (SonotaCo, 2009). An unusual concentration of four meteors was noticeable in data from 2017 October, analyzed using the UFOOrbit software. Moreover, one of these meteors had already been identified as showing an unusual physical feature, later proved to be shared by the other three (see below). Past SonotaCo data were searched for possibly associated meteors.

2 Results

Four meteors appeared from a narrow radiant area at 2017 October 26–27. Solar longitude was from 213° to 214°, on average 213°.3 (J2000.0). Mean corrected radiant position was at right ascension 328°.1 and declination +0°.4. Mean geocentric velocity was 7.4 km/s. Radiant drift was not detected. Details are shown in Table 1. Data of asteroids with similar orbits (NASA JPL, 2017) were added in Table 1. The entries in Table 1 are, from the left, time the meteor appeared (UT), solar longitude (J2000.0), corrected radiant right ascension and declination, initial velocity [km/s], geocentric velocity [km/s], a is orbital semi-major axis [AU], q is perihelion distance [AU], e is eccentricity, p is orbital period [yr], "peri" is perihelion argument, "node" is longitude of the ascending node, i is inclination, M_a is absolute magnitude and $H_{\rm beg}$ is beginning height above sea level.

The extracted meteors' corrected radiant distribution is shown in Figure 1. Data are plotted from 2007 to 2017, including all meteors having solar longitude from 206 to 221° (J2000.0), radiant right ascension from 313 to 343° and declination from −14 to +15°. In Figure 1, red circles are four Alpha Aquariid meteors. Green triangles are meteors with similar characteristics in 2007 and 2014. We can recognize sparse radiant concentrations around these meteors.

Luminous beginning height against initial velocity is shown in Figure 2 for all meteors shown in Figure 1, also shown against absolute magnitude in Figure 3. Plotting symbols are the same as in Figure 1. Alpha Aquariid meteors' beginning heights are significantly higher as indicated on Figures 2 and 3.

Alpha Aquariid meteors show the so called "melting meteor" feature. The image of the brightest meteor trail is shown in Figure 4. After half the path of the trail, the image steadily stretched to a significant length. This is discussed further in Section 3 below.

The brightest meteor (−2.4 absolute magnitude) of the Alpha Aquariids was accompanied by a persistent train that was recorded over more than one hour by the digital camera in spite of being a slow velocity meteor (initial velocity is 13.1 km/s).

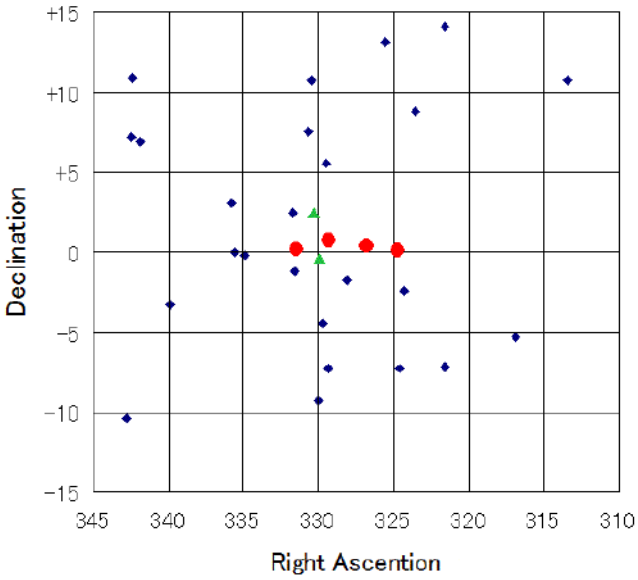

Figure 1 – Radiant distribution of Alpha Aquariids and surrounding area. Different symbols indicate Alpha Aquariids (red circles); meteors with similar characteristics in 2007 and 2014 (green triangles); and all other meteors (blue diamonds).

3 Discussion

Alpha Aquariids were identified from data on only four meteors that were not only having analogous radiant positions with similar orbits, but producing similar luminous images stretching back and forth after half of the path (Figure 4). Recorded lengthened trails are not plasma emission left behind on the luminous track which is the so called "train" and not fine pieces peeled

[1] SonotaCo Network, Japan.

IMO bibcode WGN-462-shiba-aaq
NASA-ADS bibcode 2018JIMO...46...79S

Table 1 – Alpha Aquariid meteors in 2017, similar orbit asteroids and previous similar meteors.

UT	$\lambda_\odot$	Corrected radiant		V_i	V_g	a	q	e	p	peri	node	i	M_a	H_{beg}
ymd_hms	J2000.0	R.A.	Decl	km/s	km/s	AU	AU		yr	deg	deg	deg	mag	km
20171026_120904	213.0290	331.51	+0.21	13.3	7.5	1.973	0.974	0.506	2.77	199.7	213.0	2.3	−0.7	87.0
20171026_145147	213.1417	326.79	+0.41	13.1	7.4	2.005	0.980	0.511	2.84	196.8	213.1	2.6	−2.4	96.1
20171026_151318	213.1566	324.72	+0.07	13.5	8.1	2.303	0.981	0.574	3.50	195.5	213.2	2.9	0.6	91.6
20171027_105407	213.9747	329.33	+0.72	12.9	6.6	1.781	0.979	0.451	2.38	198.0	214.0	2.3	−0.9	89.7
Average	213.3255	328.09	+0.35	13.2	7.4	1.999	0.978	0.511	2.83	197.5	213.3	2.5	−0.9	
Similar orbit asteroids		2010 UB				2.059	0.990	0.519	2.95	199.5	215.1	3.4	(NASA	
		2005 UV_6				2.143	0.987	0.540	3.14	202.1	214.2	1.9	JPL, 2017)	
Previous years meteors														
20071020_100410	206.5308	329.87	−0.49	13.4	7.2	1.828	0.970	0.469	2.47	203.1	206.5	2.2	−1.9	89.7
20141024_094519	210.7027	330.34	+2.32	13.4	7.2	1.867	0.973	0.479	2.55	201.0	210.7	2.7	−1.5	94.0

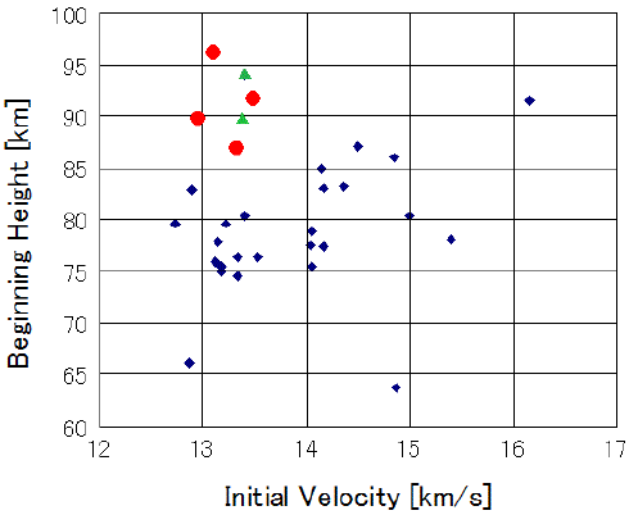

Figure 2 – Beginning height and initial velocity. Symbols as in Figure 1.

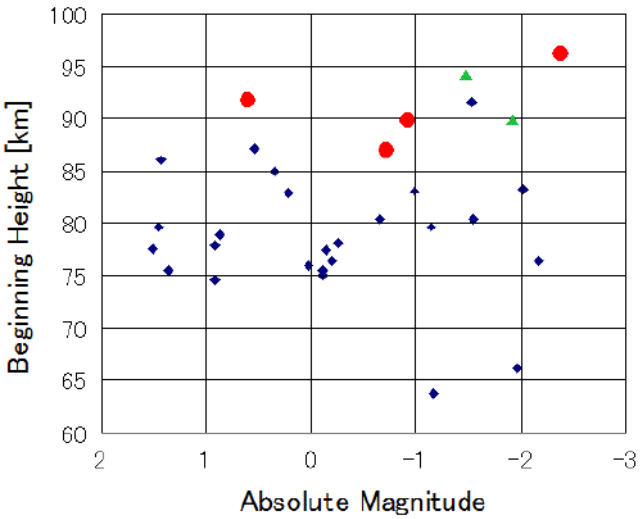

Figure 3 – Beginning height and absolute magnitude. Symbols as in Figure 1.

off from the meteoroid surface which is the so called "tail". But it was estimated that there is light from ablation by many fine, disintegrating meteoroids, occurring at an early stage in the low air density environment. As these "dustball" meteoroids give the appearance of melting away as they elongate and disintegrate, Mr. Bill Ward named this phenomenon "melting meteor" (Ward, 2016). Melting meteors correlate with high beginning heights generally and agree with the characteristics of the four Alpha Aquariid meteors. A few meteor showers include a high percentage of "melting meteors" an example being the Andromedids (Maeda, 2016). However melting meteors generally exist only at the level of a percent or less in our TV meteor observations. The possiblility is low that four "melting meteors" radiant points concentrate coincidentally. Thus, we considered that these four meteors are not sporadic meteors but a new meteor shower.

Alpha Aquariids were not recorded clearly from 2007 to 2016 in our TV observations. It is possible that Alpha Aquariids were not recorded because of clouds over their active duration spanning only a degree in solar longitude $\lambda_\odot$. We obtained more than two hundred meteor orbits from 213 to 214° in $\lambda_\odot$ in our observations in 2011 and 2017, but fewer orbits were obtained in the other nine years when the sky condition was estimated as worse. Only the last two meteors in Table 1 indicated both orbital similarity and the melting meteor feature. On the other hand, many meteors can be found in Figure 1 with similarities to Alpha Aquariid orbits. 21 of the 25 meteors in Figure 1 are indicated as Alpha Aquariid members by using the D criterion (Drummond, 1981) with threshold value 0.105. We expect that future observations will help to decide which of these meteors without the "melting meteor" feature are Alpha Aquariid members or whether they are sporadic meteors in a sparsely populated radiant region.

Equal time interval TV frame images are exhibited side by side in Figure 4 where can be seen deceleration of the meteor's angular velocity because the meteor images do not fall on a diagonal straight line. A meteoroid decomposing into fine grains will decelerate quickly by air drag. The initial velocity of meteors with unusually large deceleration is underestimated by the UFOAnalyzer automatic reduction. In this case, the calculated semi-major axis and orbital period in Table 1 indicate minimum values. If the semi-major axis is larger, the Alpha Aquariid orbits may be more similar with asteroid 2005 UV_6 than 2010 UB.

Melting meteors' inner bonding strength must be particularly weak. Therefore "melting meteors" would

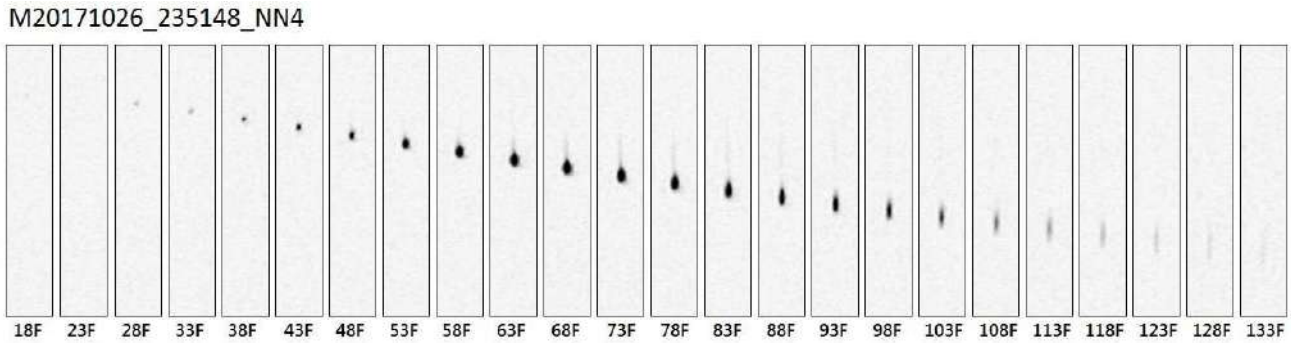

Figure 4 – Video image for each frame number. At 2017 October 26, $14^{h}51^{m}48^{s}$ (UT) taken by C. Shimoda. (Every 5th frame is shown here and the NTSC TV data are 29.97 frames/sec so that the interval is 5/29.97 seconds.)

demonstrate fragile behavior during their previous solar system existence. Meteoroid decomposition or fragmentation in the solar system can generate "cluster phenomena" (Kinoshita et al., 1999; Koten et al., 2017), that is, many meteoroids arrive in a narrow region near earth simultaneously. The four observed Alpha Aquariid meteors might be part of meteoroid fragments broken up in the solar system long ago.

Acknowledgements

Dr. Bill Ward advised us about the term "melting meteor".

References

Drummond J. D. (1981). "A test of comet and meteor shower associations". *Icarus*, **45**, 545–553.

Kinoshita M., Maruyama T., and Sagayama T. (1999). "Preliminary activity of Leonid meteor storm observed with a video camera in 1997". *Geophys. Res. Lett.*, **26**, 41–44.

Koten P., Čapek D., Spurný P., Vaubaillon J., Popek M., and Shrbený L. (2017). "September epsilon Perseid cluster as a result of orbital fragmentation". *Astron. Astrophys.*, **600**, A74, 5 pp.

Maeda K. (2016). "Melting meteors". `http://sonotaco.jp/forum/viewtopic.php?t=3630` . SonotaCo Network Japan Forum.

NASA JPL (2017). "Small-body database browser". `https://ssd.jpl.nasa.gov/sbdb.cgi` .

SonotaCo (2009). "A meteor shower catalog based on video observations in 2007–2008". *WGN, Journal of the IMO*, **37:2**, 55–62.

Ward B. (2016). "Melting meteors". `http://sonotaco.jp/forum/viewtopic.php?t=3630` . SonotaCo Network Japan Forum.

Handling Editor: David Asher

Visually estimating directions of meteors from static images: Possible or not?

Andreas Buchmann[1,2], *Stefan Meister*[1], *and Martin Dubs*[1]

On static images of meteor trails it is generally not possible to unambiguously determine their directions. We had six volunteers guess the directions of meteors on such images and asked them for strategical cues which helped them to make a decision. We calculated how helpful the strategies were by comparing the guessed directions with the actual directions. We found two classes of strategies that were partly complementing each other. A singular strategy that worked the best dictated that the brightest point of a meteor should be located after the middle of the trail (true in 72% of the cases) because meteors brighten slowly and fade quickly, while the other concerned the morphology of the trail (flares occur towards the end). Combining these strategies, the volunteers were able to estimate the direction correctly in 77% (median) of the cases. We also discuss physics of meteors which may influence the applicability of these strategies.

Received 2018 February 20

1 Introduction

What was the flight direction of the meteor in Figure 1? Two of us (A.B., S.M.) stumbled over this question while fitting meteor direction vectors in video data. Unfortunately, the direction information cannot be assessed from a conventional photograph, unless tracked by eye or a video system in parallel. Looking at a picture, it is not clear if the meteor was going from the top to the bottom, or the other way around. To investigate if a person can properly guess the correct direction, and on which knowledge they base their decision, we employed 6 volunteers, to which were presented 100 coadded meteor video frames. We then compared their guesses with known directions. Furthermore, we asked the volunteers to describe strategies they used, and we have assessed the success of individual strategies. We were aware that this study would not yield a deterministic formula that would always correctly predict the direction, but rather some probabilistic proxies that are valid in most cases.

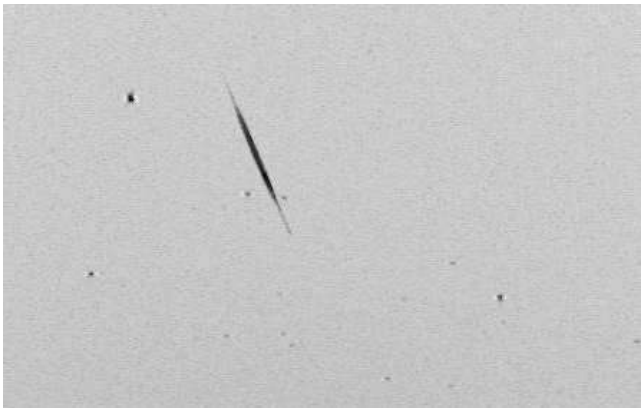

Figure 1 – An example meteor trail (inverted image) that was used along with 99 other meteor trails.

2 Methods

For the first part of the study (strategy finding), 100 videos were selected from over 1500 obtained between November 2014 and October 2015 using three Watec 902H Ultimate cameras. The cameras were oriented towards the north, south east and south west. The recording was done using UfoCapture 2.23 software[a]. The videos were chosen in such a way that all directions of flight had the same number of occurrences (e.g. the same number bottom-right to top-left as top-left to bottom-right), and the images were cropped to remove the horizon and obvious constellations. The images were presented to the volunteers (S.M., M.D., and four additional volunteers) in an individualised pseudorandom sequence. We have sorted the meteors by their direction, the part of the night when they occurred (before or after 23^h00^m UTC, corresponding to 00^h00^m local time in winter, and 01^h00^m local time in the summer), camera pointing direction (N, SE, SW) and the number of sudden increases in brightness (flares). Out of the 100 used meteors, 67 had been processed with UfoAnalyzer, thus the shower association, the magnitude, duration, as well as the coordinates of beginning and end points were known for those cases. The volunteers also gave a confidence rating (1 = worst, 6 = best) to the estimated flying direction.

To compare the predictions of strategies A, B1 and B2, we used a larger dataset consisting of images of 965 shower meteors collected between 2014 November 19 and 2017 July 31 with 7 different Watec cameras. First, we classified the directions according to strategies A, B1 and B2, and then determined the actual directions by looking at videos.

3 Results

All 6 volunteers used the strategy A, which used the assumption that a meteor brightens slowly and fades quickly, the brightest point being close to the end of the meteor. This strategy yielded 72 correct and 20 wrong directions but was not applicable in 8 cases, because the brightness peak was very close to the middle of the trail (as rated by the author). The other strategies used by volunteers are listed in Table 1.

[1]Fachgruppe Meteorastronomie, Swiss Astronomic Society (SAG)
[2]Email: andreasbuchmann@hotmail.com

IMO bibcode WGN-462-buchmann-directions
NASA-ADS bibcode 2018JIMO...46...82B

[a]UfoCapture: http://sonotaco.com

Table 1 – Strategies used by volunteers

Strategy	Description	No. of volunteers that used the strategy
A	Meteor brightens slowly, fades quickly (the brightest point towards the end of the trail)	6 (all)
B1	Flares will preferably occur towards the end of the trail.	3, one said the brightening should happen in the middle
B2	The width increases towards the end of the trail.	1
C1	Downward direction more likely than upward.	2
C2	From left to right more likely than from right to left.	1

We note that C strategies were not valid in the actual meteor sample, as the direction of the meteors was chosen to be uniform. Nevertheless, in a more realistic setting strategy C might have had a probabilistic advantage due to a possible radiant of an active meteor shower. One additional strategy not mentioned by the volunteers 'D' could be added, namely 'long meteors tend to come from the apex' (not discussed further in this article). The volunteers had a similar success rate: they were correct in 70, 75, 76, 77, 78 and 79 cases, out of 100. Also, on average the volunteers had a high degree of confidence in meteors for which they guess the direction correctly. The median confidence for correct guesses was 3.96, while for wrong guesses it was only 2.56. We note that the confidence was higher if the volunteers were able to successfully apply the strategy A (3.96) than if they were not (2.14). Thus, including meteors for which strategy A did not apply resulted in a higher median confidence.

We also calculated the success rate of the majority's vote on the direction. The majority was right in 76 out of 93 meteors (7 were not counted because 3 volunteers opted for one, and the other three volunteers for the other prediction). Our result was comparable to single volunteer predictions, the median of all six volunteers was 76.5 out of 100 meteors.

By analyzing meteors and their known directions, strategy A yielded 72 correct ratings. This number is relatively close to the number of correct ratings achieved by our volunteers, who did better than this average. The confidence ratings were higher for cases where the strategy was applicable, 2.15 ± 0.19, compared to 2.77 ± 0.2 for cases where the strategy was not applicable. This shows that the volunteers strongly adhered to rule A – they used it in in about 80% of the cases.

We tried to determine in which cases the rule works, and in which it does not work, comparing meteors with correct versus wrong prediction by strategy A. Strong correlations were observed for meteor brightness, pointing direction of the camera and the portion of the night (note that these three variables are strongly interconnected, since morning meteors tend to be fast, brighter and occur in the east), but no statistically significant conclusions could be made. For the five volunteers who had more correct guesses than the predicted number by only following strategy A, using another strategy was more often successful. For example, sometimes the form strategy B2 contradicts the brightness strategy A, as seen on Figure 1. In this example, the maximum brightness is at the bottom, whereas the meteor has a larger width at the top. 4 out of 6 volunteers correctly assessed that the meteor was going downwards using strategies A and/or C1, while 2 said it was going upwards using strategy B2.

In the second part of the study designed to check the strategies derived from the first part in a larger sample of shower meteors, strategy A was correct in 83.8% of the cases, rule B1 only in 8.3%, and rule B2 in 63.0%. If the strategies were applicable, they were correct in the following proportion of cases: A in 90.1%, B1 in 98.8%, B2 in 91.9%. This means that the most often applicable strategy (A) was the least reliable, whereas the least often applicable strategy (B1, flares at the end of the trail) was the most reliable in the applicable cases, which were few. Strategies A and B2 showed a large overlap in applicability and accuracy. Comparing strategies A and B1, they showed the same information content (both correct, both no prediction, or both wrong) in 23.3% of cases. In the remaining 76.7%, strategy A clarifies no cases at all in which rule B1 is unclear or incorrect, whereas the strategy B1 clarifies 11 out of 84 cases (13.1%) in which rule A is unclear or incorrect. This means that rules A and B1 could be combined.

4 Discussion of possible physical causes

Öpik (1958) made theoretical calculations of flights of meteors in the atmosphere under the assumption of an exponential air pressure decrease with increasing height and constant meteor speed. He estimated that the point of maximal brightness should be roughly 6 km above than the end of the luminous path, i.e. rather towards its end. The conclusion was demonstrated to be independent from the entrance angle and speed (note that very bright and fragmenting meteors may behave differently). This seems to parallel strategy A in many cases (i.e. in small and not fragmenting meteoroids). For fragmenting meteoroids, which may be rather the rule than the exception (Subasinghe et al., 2016), sudden gross fragmentation may lead to flares, and continuous fragmentation into finer grains may also influence the light curve (Campbell-Brown, 2017).

5 Conclusions

We have shown that visually classifying the direction of meteor on static images produces correct guesses in 3/4 of the cases; this number is higher for bright meteors, for meteors in the morning sky, and for meteors

in the east, probably because fast/apex source meteors are easier to classify. We have found three types of functional strategies: A - the meteor should be brighter in the second half of the trail; B - the meteor should be wider in the second half of the trail and/or have more flares there. We show that strategy A is mostly applicable and most often correct. B2 ('width increases towards the end of the trail') strongly overlaps with A and gives almost no additional information, whereas B1 ('flairs preferably towards end of the trail'), if applicable, is almost always correct (84 correct versus 1 wrong cases). Using the strategy B1 in cases where it makes a prediction, adds information and accuracy to just using A. Our best combined strategy would consequently be 'if there is flare use strategy B1, otherwise A', which leads to 76.6% correct predictions, which corresponds well to the average of correct responses of the 6 volunteers in a smaller sample of meteors. We also calculated which features of meteors corresponded to correct versus wrong predictions for each strategy and found that brighter meteors produced more accurate predictions using all three strategies, whereas a long meteor duration only helped strategy B1. Interestingly, faster speeds produced more accurate predictions using strategies A and B2, whereas strategy B1 worked best for low speeds. This was because flares were only seen in low-speed meteors. Finally, we conclude that a 100% accuracy cannot be reached visually, but in general flares tend to occur towards the end, and that the brightest and the widest part of the trail corresponds to the end of the meteor as well.

6 Acknowledgements

The authors would like to thank the four volunteers from the Swiss 'Fachgruppe Meteorastronomie', and the handling editor Denis Vida for his insightful comments.

References

Campbell-Brown M. (2017). "Modelling a short-wake meteor as a single or fragmenting body". *Planetary and Space Science*, **143**, 34–39.

Öpik E. (1958). "Physics of meteor flight in the atmosphere, No. 6 in Interscience tracts on physics and astronomy".

Subasinghe D., Campbell-Brown M. D., and Stokan E. (2016). "Physical characteristics of faint meteors by light curve and high-resolution observations, and the implications for parent bodies". *Monthly Notices of the Royal Astronomical Society*, **457:2**, 1289–1298.

Handling Editor: Denis Vida

Short communication

February Hydrids outburst (IAU#1032, FHY)

Peter Jenniskens[1], *Carl Johannink*[2], *and Nick Moskovitz*[3]

The CAMS video meteoroid orbit survey detected a Jupiter-family comet type outburst from a geocentric radiant at R.A. = 123.°9, Dec. = +1.°5 and speed V_g = 16.4 km/s in the period 2018 February 9–17. The shower is new to the IAU Working List of Meteor Showers. There is no known parent body.

Received 2018 April 3

During routine operation of the CAMS video meteoroid survey (Jenniskens et al., 2011), a small excess of 17 meteors over the sporadic background was detected from a geocentric radiant at R.A. = 123.°9±1.°2, Dec. = +1.°5 ± 1.°2, in the constellation Hydra, and a speed $V_g = 16.4 \pm 1.3$ km/s during 2018 February 9–17 (Figure 1). Orbits are listed in Table 1, together with median values and the 1-σ standard deviation from the mean. Most meteors were observed on two nights at solar longitude 323°and 324°. The median orbital elements are those of a low-inclined Jupiter-family comet with semi-major axis $a = 2.68 \pm 0.32$ AU (error in the median value, the standard deviation dispersion is 1.34 AU). The shower was not detected in previous years and was not previously reported to the IAU Meteor Shower Working List (Jopek & Kanuchova, 2014), suggesting this was a meteor outburst.

A possible parent body is the H = 19.9 magnitude Near Earth Object 2002 MT_3, but the agreement in orbital elements is poor. The nodal line is rotated by about 25° and the perihelion distance is higher. Other candidates include 28442 (2006 YD) and 2000 YN_{29}. A more likely candidate may yet be discovered.

CAMS is supported by the NASA NEOO program. We thank the many amateur astronomers who operate the CAMS stations and obtained this data.

[1]SETI Institute, Mountain View, California. USA.
Email: petrus.m.jenniskens@nasa.gov
[2]CAMS BeNeLux
[3]LO-CAMS, Lowell Observatory, Flagstaff, Arizona

IMO bibcode WGN-462-jenniskens-fhy
NASA-ADS bibcode 2018JIMO...46...85J

References

Jenniskens P., Gural P. S., Dynneson L., Grigsby B., Newman K. E., Borden M., Koop M., and Holman D. (2011). "CAMS: Cameras for Allsky Meteor Surveillance to establish minor meteor showers". *Icarus*, **216**, 40–61.

Table 1 – Orbital elements of February Hydrids. Network: 1 = California, 3 = BeNeLux, 6 = LO-CAMS.

$\lambda_\odot$ (°)	RA_g (°)	Dec_g (°)	V_g (km/s)	q (AU)	a (AU)	e	i (°)	ω (°)	Node (°)	Π (°)	Network
321.34	121.52	+3.05	18.77	0.793	4.32	0.816	8.63	55.70	141.34	197.04	1
322.14	122.32	+2.83	16.55	0.810	2.74	0.704	7.79	55.52	142.14	197.66	1
322.22	122.92	+2.61	16.02	0.811	2.47	0.672	7.65	56.22	142.22	198.44	1
323.29	123.05	+2.07	16.36	0.814	2.68	0.697	7.96	55.07	143.29	198.36	1
323.32	123.44	+2.81	17.39	0.804	3.17	0.747	8.02	55.62	143.31	198.93	1
323.82	123.92	+1.86	16.34	0.812	2.62	0.691	7.98	55.62	143.81	199.43	3
323.99	123.76	+1.93	16.12	0.816	2.58	0.684	7.85	55.13	143.98	199.11	3
324.29	123.99	+1.44	16.33	0.814	2.65	0.693	8.13	55.13	144.28	199.42	1
324.33	124.56	+3.22	20.40	0.780	7.87	0.901	8.80	56.11	144.33	200.44	1
324.81	124.10	+1.08	16.43	0.816	2.73	0.701	8.30	54.66	144.80	199.46	3
324.94	123.61	+1.12	18.31	0.806	4.11	0.804	9.08	54.03	144.94	198.97	3
324.97	124.84	+1.48	16.92	0.808	2.89	0.720	8.28	55.49	144.97	200.45	3
324.98	125.69	+1.00	15.64	0.813	2.30	0.646	7.91	56.60	144.98	201.57	3
325.08	126.17	+0.97	16.79	0.801	2.64	0.697	8.39	57.29	145.08	202.37	6
325.20	123.45	−0.08	15.88	0.827	2.59	0.680	8.56	53.31	145.20	198.51	1
326.40	124.00	−0.42	15.21	0.835	2.40	0.652	8.31	52.48	146.40	198.88	1
327.13	125.43	−0.33	16.40	0.822	2.78	0.704	8.71	53.65	147.13	200.78	1
324.33	123.92	+1.48	16.40	0.812	2.68	0.697	8.28	55.49	144.33	199.11	**Median**
±1.49	±1.18	±1.15	±1.28	±0.012	±1.34	±0.065	±0.40	±1.22	±1.49	±1.37	**1-σ**
328.28	*120.85*	*+4.46*	*14.46*	*0.867*	*2.80*	*0.691*	*6.52*	*25.27*	*168.46*	*193.73*	**2002 MT_3**

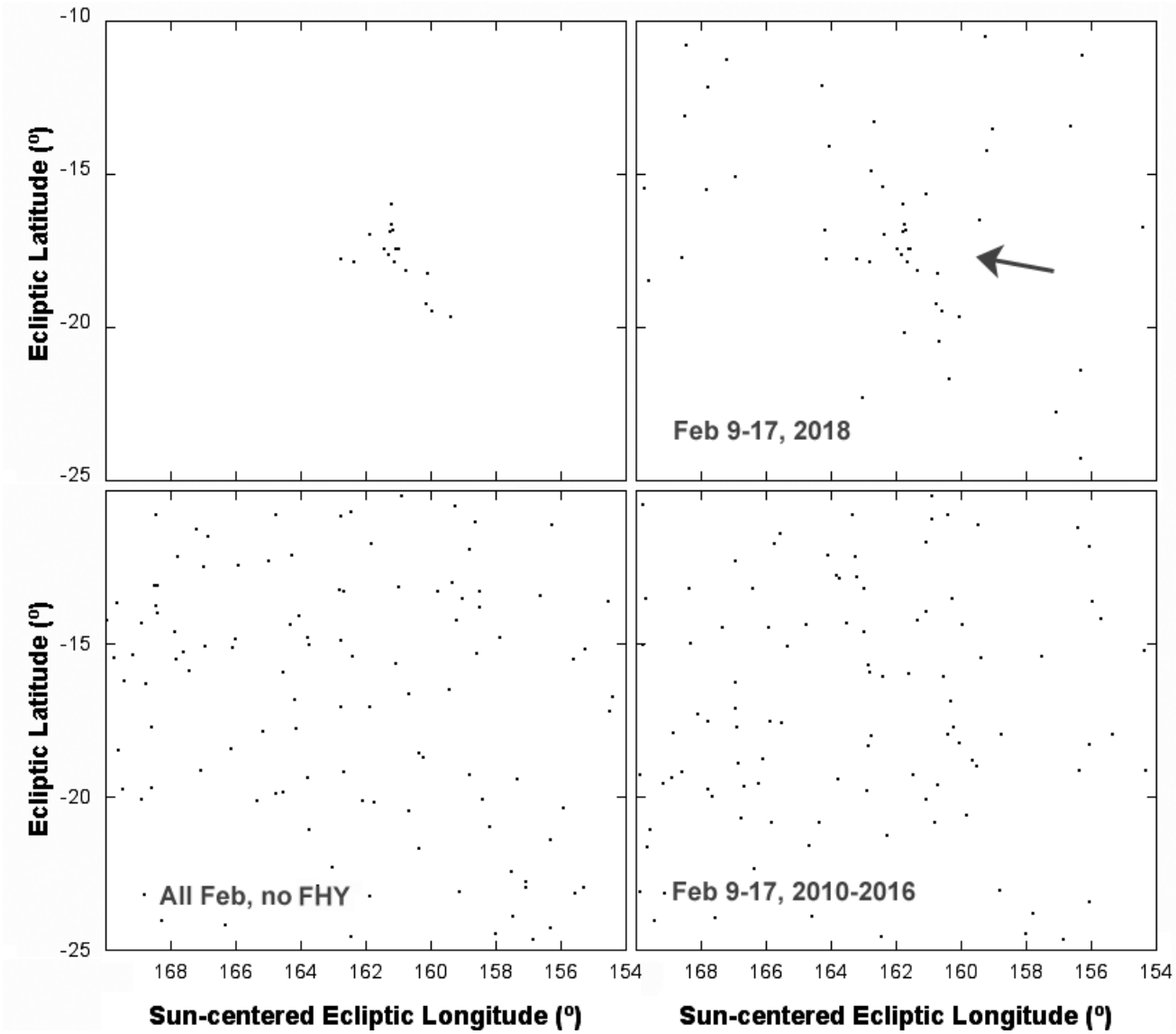

Figure 1 – Top right: Radiant distribution in sun-centered ecliptic coordinates for meteors detected in the period 2018 February 9–17. Arrow points to the February Hydrids (isolated in the top left figure). Bottom left diagram shows all meteors detected in 2018 February, while the bottom right diagram shows all CAMS detected meteors from previous years during February 9–17.

Jopek T. J. and Kanuchova Z. (2014). "Current status of the IAU MDC Meteor Showers Database". In Jopek T. J., Rietmeijer F. J. M., Watanabe J., and Williams I. P., editors, *Proceedings of the Meteoroids 2013 meeting. A. M. University, Poznan, Poland, Aug. 26-30, 2013*. A. M. University Press, pages 353–364.

Handling Editor: Javor Kac

The International Meteor Organization

www.imo.net

Follow us on Facebook
InternationalMeteorOrganization

Follow us on Twitter
@IMOMeteors

Council

President: Cis Verbeeck,
Bogaertsheide 5, 2560 Kessel, Belgium.
e-mail: cis.verbeeck@scarlet.be

Vice-President: Juraj Tóth,
Fac. Math., Phys. & Inf., Comenius Univ.,
Mlynska dolina, 84248 Bratislava, Slovakia.
e-mail: toth@fmph.uniba.sk

Secretary-General: Robert Lunsford,
14884 Quail Valley Way, El Cajon,
CA 92021-2227, USA. tel. +1 619 755 7791
e-mail: lunro.imo.usa@cox.net

Treasurer: Marc Gyssens, Heerbaan 74,
B-2530 Boechout, Belgium.
e-mail: marc.gyssens@uhasselt.be
BIC: GEBABEBB
IBAN: BE30 0014 7327 5911
Bank transfer costs are always at your expense.

Other Council members:

Megan Argo, Jodrell Bank Centre for Astrophysics,
Alan Turing building, University of Manchester,
Oxford Road, Manchester, M13 9PL, UK.
e-mail: megan.argo@gmail.com

Javor Kac (see details under WGN)

Detlef Koschny, Zeestraat 46,
NL-2211 XH Noordwijkerhout, Netherlands.
e-mail: detlef.koschny@esa.int

Masahiro Koseki, 4-3-5 Annaka, Annaka-shi,
Gunma-ken 379-0116, Japan.
e-mail: geh04301@nifty.ne.jp

Sirko Molau, Abenstalstraße 13b, D-84072 Seysdorf,
Germany. e-mail: sirko@molau.de

Jean-Louis Rault, Société Astronomique de France,
16, rue de la Vallée, 91360 Epinay sur Orge,
France. e-mail: f6agr@orange.fr

Jürgen Rendtel, Eschenweg 16, D-14476 Marquardt,
Germany. e-mail: jrendtel@aip.de

Paul Roggemans, Pijnboomstraat 25, 2800 Mechelen,
Belgium, e-mail: paul.roggemans@gmail.com

Galina Ryabova, Res. Inst. of Appl. Math. & Mech.,
Tomsk State University, Lenin pr. 36, build. 27,
634050 Tomsk, Russian Federation.
e-mail: ryabova@niipmm.tsu.ru

Damir Šegon, J. Rakovca 3, 52100 Pula, Croatia.
e-mail: damir.segon@pu.t-com.hr

Commission Directors

Visual Commission: Rainer Arlt (rarlt@aip.de)
Generic e-mail address: visual@imo.net
Electronic visual report form:
http://www.imo.net/visual/report/electronic

Video Commission: Sirko Molau (video@imo.net)

Photographic Commission: Bill Ward
(William.Ward@glasgow.ac.uk)
Generic e-mail address: photo@imo.net

Radio Commission: Jean-Louis Rault (radio@imo.net)

Fireballs: Online fireball reports:
http://fireballs.imo.net

Outreach Officer

Jure Atanackov, e-mail: jureatanackov@gmail.com

Webmaster

Karl Antier, e-mail: webmaster@imo.net

WGN

Editor-in-chief: Javor Kac
Na Ajdov hrib 24, SI-2310 Slovenska Bistrica,
Slovenia. e-mail: wgn@imo.net;
include METEOR in the e-mail subject line

Editorial board: Ž. Andreić, M. Argo, D.J. Asher,
F. Bettonvil, J. Correira, M. Gyssens,
C. Hergenrother, T. Heywood, J.-L. Rault,
J. Rendtel, C. Verbeeck, S. de Vet, D. Vida.

IMO Sales

Available from the Treasurer or the Electronic Shop on the IMO Website	€	$
IMO membership, including subscription to WGN Vol. 46 (2018)		
Surface mail	26	35
Air Mail (outside Europe only)	49	65
Electronic subscription only	21	25
Proceedings of the International Meteor Conference on paper		
1990, 1991, 1993, 1995, 1996, 1999, 2000, 2002, 2003, per year	9	12
2007, 2010, 2011, per year	15	20
2012, 2013, 2014, 2015 per year	25	34
Proceedings of the Meteor Orbit Determination Workshop 2006	15	20
Radio Meteor School Proceedings 2005	15	20
Handbook for Meteor Observers	15	20
Meteor Shower Workbook	12	16
Electronic media		
Meteor Beliefs Project ZIP archive	6	8

2018 Lyrids

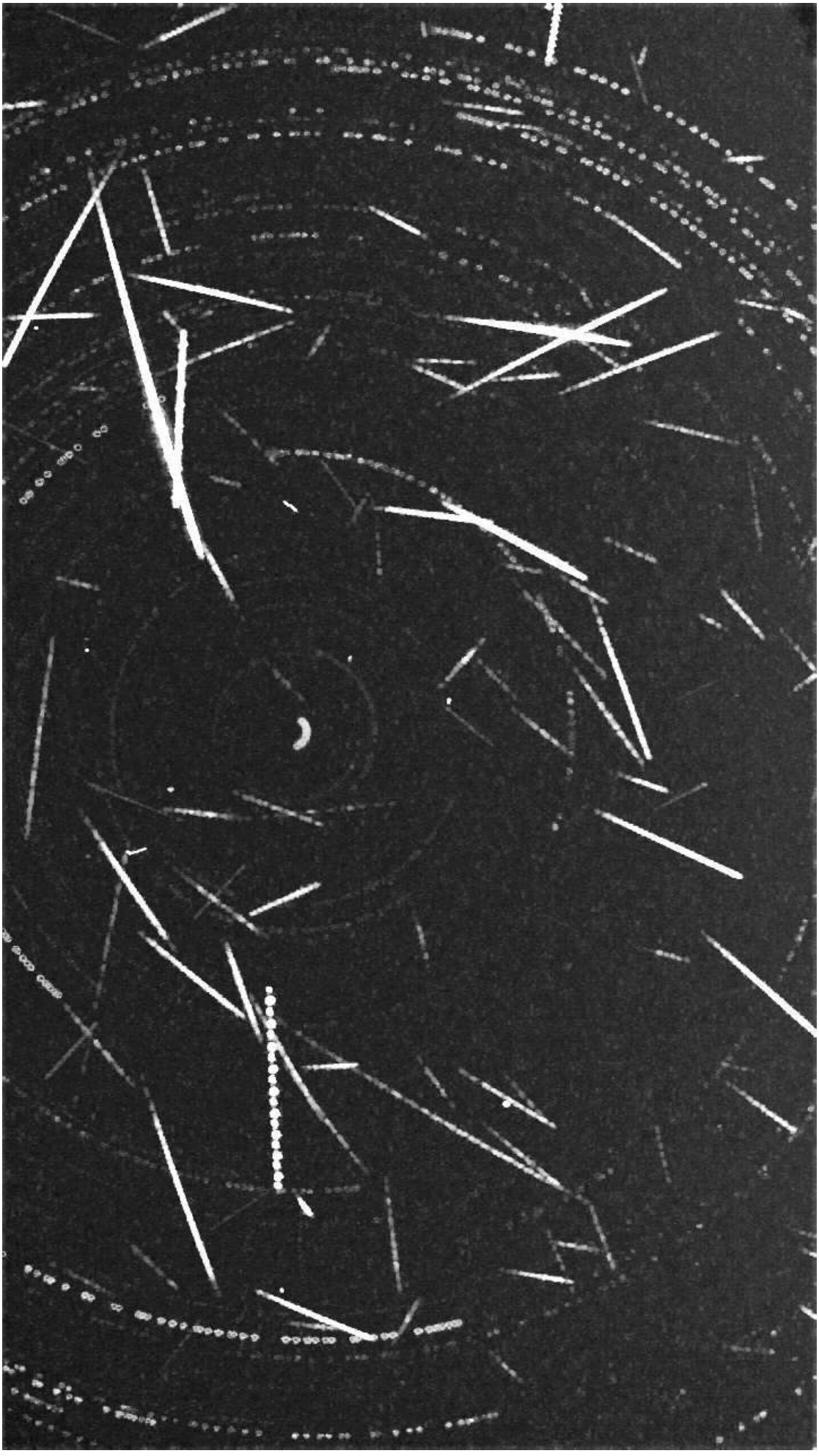

Composite of 102 Lyrids detected on 2018 April 21–23 using an IMX225 IP camera (4 mm $f/1.2$ lens) on a Raspberry Pi 3 with RMS software from Elginfield, Ontario, Canada. Image credit: Denis Vida.